

Microscopic modeling of tunneling spectra in $\text{Bi}_2\text{Sr}_2\text{Ca}_2\text{Cu}_3\text{O}_{10+\delta}$ (Bi-2223)

C. Berthod, Y. Fasano,* I. Maggio-Aprile, A. Piriou, E. Giannini, G. Levy de Castro,† and Ø. Fischer
DPMC-MaNEP, Université de Genève, 24 quai Ernest-Ansermet, 1211 Genève 4, Switzerland

(Dated: 11 March 2013)

We study a series of spectra measured in the superconducting state of optimally-doped Bi-2223 by scanning-tunneling spectroscopy. Each spectrum, as well as the average of spectra presenting the same gap, is fit using a microscopic model that takes into account the band structure, the BCS gap, and the interaction of electrons with the spin-resonance mode. After describing our measurements and the main characteristics of the strong-coupling model, we report the whole set of parameters determined from the fits, and we discuss trends as a function of the gap magnitude. We also simulate angle-resolved photoemission spectra using the parameters resulting from our fits, and compare with recent experimental data.

PACS numbers: 74.72.-h, 68.37.Ef, 74.25.Jb, 74.50.+r

I. INTRODUCTION

The two main single-electron spectroscopies, angle-resolved photoemission¹ (ARPES) and scanning tunneling microscopy² (STM), have been considerably improved during the last two decades, largely motivated by the need for ever more reliable data in the study of cuprate high-temperature superconductors. Thanks to a steady improvement in the sample quality, a rapidly growing body of high-quality spectroscopic data is now available for the cuprates, especially for compounds with easily-obtained clean surfaces as the Bi-based family. These refined experiments on high-quality crystals seem now able to deliver the intrinsic line-shape of the one-electron spectra. Nonetheless, very few studies have so far undertaken a detailed line-shape study of the various spectral features, by means of a microscopic model. In previous works, the STM data analysis remained largely qualitative, or based on phenomenological approaches. In a few cases, a BCS d -wave model including a realistic band structure,³ and/or a phenomenological scattering rate,⁴ turned out to be appropriate. Such cases are the exception rather than the rule: these simple models will not capture, in particular, a structure ubiquitously present at energies above the superconducting gap, the “dip” feature. By analogy with phonon-related effects in classical superconductors,^{5,6} the dip, which has also recently been observed in pnictide superconductors,^{7,8} is generally attributed to a collective mode.

The cuprates present, in their superconducting phase, a low-energy magnetic excitation known as the spin resonance. This excitation emerges below the superconducting critical temperature, T_c , as a strong enhancement of the spin susceptibility around the anti-ferromagnetic vector $\mathbf{Q} = (\pi/a, \pi/a)$. First discovered in the inelastic neutron scattering response of $\text{YBa}_2\text{Cu}_3\text{O}_{6+x}$ ^{9,10} (Y-123) at an energy of $\Omega_s = 41$ meV, it has been observed since then in most cuprates, including the single-layered compounds $\text{HgBa}_2\text{CuO}_{4+\delta}$ ¹¹ and $\text{Tl}_2\text{Ba}_2\text{CuO}_{6+\delta}$,¹² the two-layer $\text{Bi}_2\text{Sr}_2\text{CaCu}_2\text{O}_{8+\delta}$ (Bi-2212),¹³⁻¹⁵ and the electron-doped material $\text{Pr}_{0.88}\text{LaCe}_{0.12}\text{CuO}_{4-\delta}$.¹⁶ The (π, π) resonance is detected at energies ranging from 10 to 60 meV, roughly correlated with T_c following the dependence $\Omega_s \approx 5.3k_B T_c$.¹⁷ It is found in both underdoped and overdoped materials,¹⁸

and was also detected above T_c in Y-123.¹⁹ The resonance has been interpreted as the signature of a spin-1 exciton, a bound state below the continuum of electron-hole excitations, gapped by the superconducting pairing.²⁰ One of the theoretical questions, that remains unsettled so far, concerns the role played by spin fluctuations, and particularly by the (π, π) resonance, in the pairing phenomenon.^{21,22}

Being related to superconductivity or not, the (π, π) resonance is a collective spin mode, which must somehow interact with the charge degrees of freedom, and induce renormalization and damping of the Bogoliubov quasiparticles in the superconducting state. Such effects certainly modify the one-electron spectra, and are in principle observable in single-electron spectroscopies. Although the strength of this interaction has been the matter of a controversy,^{23,24} there is now enough evidence that peculiar signatures observed in photoemission,²⁵⁻²⁸ tunneling,²⁹⁻³³ and optical conductivity^{34,35} result from this interaction. Nevertheless, a firm consensus has not been reached yet: optical phonons are often present in the cuprates at nearly the same energies than the spin resonance, and discriminating unequivocally the effects of the two kinds of excitations has proven difficult. The spin resonance, being localized near (π, π) , naturally leads to an anisotropic scattering rate and a strong dip.³¹ But similar effects can also be induced by phonons, provided that the electron-phonon coupling is strongly anisotropic.³⁶ A possible way of understanding the origin of the dip feature is to study its evolution as a function of doping, and to compare it with the doping-dependence of the spin resonance and of the phonons, both directly measured by neutron scattering.

In a d -wave superconductor, one of the signatures of the coupling to a collective mode is a *minimum*, so-called dip, in the electron density of states (DOS), occurring at an energy E_d , which is separated from the energy Δ_p (of the coherence peak) by the mode energy,³⁷ $E_d = \Delta_p + \Omega_s$. In contrast, for s -wave superconductors, the signature is a *change of curvature* of the DOS, leading to a peak in the DOS derivative.^{38,39} Scanning tunneling microscopy/spectroscopy (STM/STS) probes the electron local DOS (LDOS) with sub-meV and atomic resolutions.² It enables to locally measure the d -wave gap in the electron excitation spectrum, as well as the dip, and to track their spatial variations in inhomogeneous

materials.³² It is therefore an ideal tool to investigate the properties of the dip, and the relationship between the gap and the spin-mode energy.

Among the cuprates, the three-layered compound $\text{Bi}_2\text{Sr}_2\text{Ca}_2\text{Cu}_3\text{O}_{10+\delta}$ (Bi-2223) is probably the best-suited material to perform such studies. Like other members of the Bi-family, it can be easily cleaved, and offers atomically-flat surfaces for STM investigations. Bi-2223 has the highest optimal T_c of the Bi-family, 111 K, a gap in the 30–60 meV range, and a very strong dip as revealed by tunneling⁴⁰ and photoemission^{41–43} studies.

In this paper, we study Bi-2223 STS spectra by means of least-square fits, with a microscopic model³⁷ containing the three ingredients required to reproduce the experimental data: the Van Hove singularity of a tight-binding band, a d -wave BCS gap, and a coupling to the (π, π) spin resonance. The results of similar previous studies were already reported.^{31,32} Here, we describe our fits with full detail, provide and discuss the complete set of parameters determined from the fits, and fit average as well as local individual spectra. Our motivation for performing direct fits to cuprate STS data is two-fold. The first aim is to demonstrate that, in spite of its simplicity, the model captures quantitatively the main characteristics of the tunneling spectra for optimally-doped Bi-2223: a V-shaped gap at low energies, tall coherence peaks and very pronounced dips, both features noticeably electron-hole asymmetric. Second, the good quality of these fits provides further evidence that the STM tunneling conductance measures the full *electron* LDOS,³ rather than an effective quasiparticle DOS deprived of band-structure and self-energy effects.⁴⁴

In Sec. II, we describe the growth and characterization methods of the samples used for this study, present the measurement method, and discuss the main features of the spectra. Section III is dedicated to the model used to fit the data. We use slightly different conventions than Ref. 37 for defining the model parameters: for clarity, we therefore describe and discuss our model in detail. We also explain our fitting method. In Sec. IV, we present our results and the trends in parameters deduced from the fits. We discuss the values of the most important parameters in Sec. V, compare with those obtained using other experimental techniques, and present simulations of ARPES intensities. Finally, we summarize the main results and the implications of the present study in Sec. VI.

II. EXPERIMENTAL DETAILS

A. STM measurements, sample growth and characterization

The LDOS measurements were performed by means of a home-built STM with ultra-high vacuum environment, and ³He base temperature.⁴⁵ Electrochemically-etched iridium tips served as the ground electrode, and a bias-voltage V was applied to the sample. Therefore, negative (positive) bias refers to occupied (empty) sample states. Differential-conductance spectra, dI/dV , were directly acquired using a

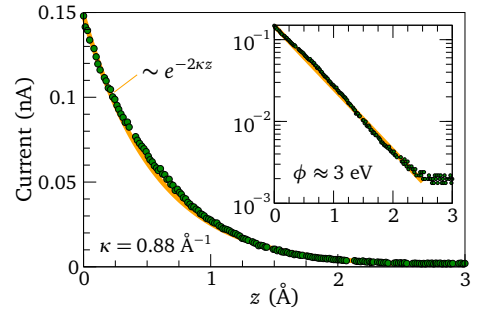


FIG. 1. Exponential decay of the tunnel current with increasing the relative tip-sample distance z , for one of our typical junctions. These data were obtained in a measurement with the current feedback-loop open. Inset: same data on a logarithmic scale.

lock-in technique.² All the dI/dV measurements reported here were performed at fixed tip-sample distance, determined by regulation current and voltage of 0.6 nA and 600 mV, and a lock-in excitation amplitude of 2 mV.

The samples were cleaved at room temperature at $1-5 \times 10^{-9}$ mbar pressure, and cooled down to 2 K in 10 hours time. In this way, high-quality tunnel junctions were typically obtained, as revealed by the data shown in Fig. 1. In a high-quality tunnel junction, the current depends exponentially on the relative tip-sample distance, z , namely $I \propto e^{-2\kappa z}$. The decay constant κ is related to the apparent barrier height $\phi = \hbar^2 \kappa^2 / (2m)$. Our tunnel junctions have typically $\phi = 3-4$ eV, much larger than the regulation voltage. We started all our runs of measurements by performing tests like the one shown in Fig. 1.

The Bi-2223 crystals were grown by the traveling-solvent floating-zone method, as described in Ref. 46. In order to achieve optimal doping, the crystals were annealed during 10 days at 500°C under an oxygen partial pressure of 20 bar. This thermal treatment produced a sharpening of the superconducting transition with respect to the as-grown condition. Figure 2(a) shows the low-field susceptibility ver-

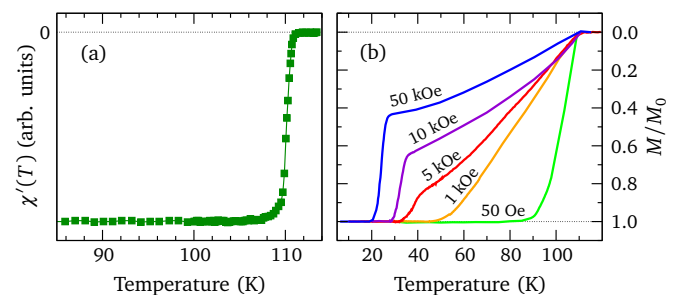


FIG. 2. Magnetic properties of an optimally-doped Bi-2223 crystal from the same batch as the one used for STM studies. (a) Real part of the magnetic susceptibility as a function of temperature, revealing a $T_c = (110.5 \pm 0.5)$ K. Measurements were performed with an ac field of 0.1 Oe and 970 Hz. (b) Temperature evolution of the magnetization in field-cooling processes at various applied fields. The magnetization is shown normalized by the low-temperature saturation value M_0 .

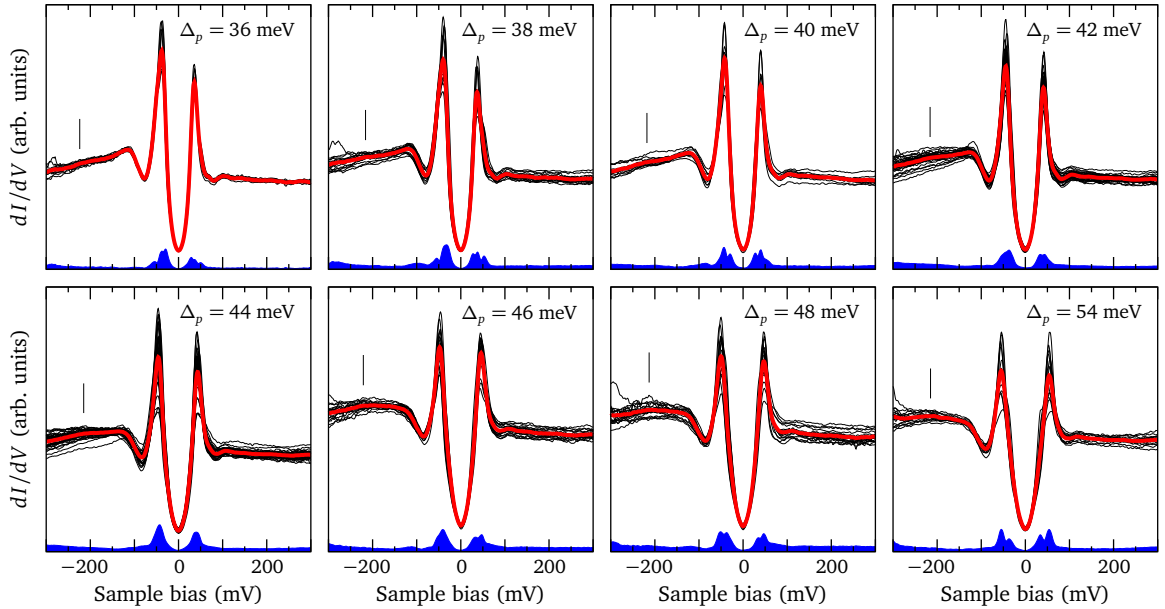


FIG. 3. The complete experimental dataset considered in this study. The raw Bi-2223 tunneling conductance spectra were grouped according to their peak-to-peak gap Δ_p , and were normalized in order to have the same spectral weight in the range of the figure (black curves). The red curves are the average spectra, and the shaded blue curves show the standard deviation of the distribution of tunneling conductances at each bias. The vertical bars indicate a weak feature, possibly related to the Van Hove singularity of the inner-layer band (see Sec. III).

sus temperature for a typical optimally-doped (OPT) sample, with a critical temperature $T_c = (110.5 \pm 0.5)$ K.⁴⁷ We considered the peak position in the temperature derivative of the low-field susceptibility and magnetization data as the criteria to determine T_c . Both determinations yielded the same T_c . The transition width, estimated as the FWHM of the susceptibility and magnetization peaks, typically ranges between 0.6 and 2 K from sample to sample.

The structural and superconducting properties of OPT crystals of the same batch than the ones studied here are reported in Refs 47–50. X-ray diffraction measurements have revealed the purity and the high crystalline order of the samples.⁴⁹ Electrical resistivity data also revealed a single and sharp superconducting transition. The sample-growing and thermal-treatment parameters were optimized, in order to suppress the intergrowth of the Bi-2212 phase in the three-layered compound. For the case of the OPT samples studied here, Bi-2212 intergrowth, if present, represent less than 1% of the sample volume.⁴⁷

B. Data statistics and systematics of spectral features

As largely documented in the literature, Bi-based cuprate samples, even with a sharp superconducting transition, present inhomogeneous spectroscopic properties on the surface at the nanoscale.² In a previous work,³² we mapped the local dI/dV curves in order to study the nanoscale variations of typical spectral features. In particular, we found that the local value of the superconducting gap measured by Δ_p presents spatial variations in register with the crystalline

structure.

The present paper is focused on studying relevant spectral features as a function of Δ_p . Since results in several OPT samples are similar, for the present study we considered 150 spectra measured at different locations of a given OPT sample. The local dI/dV curves were sorted by half the peak-to-peak energy separation, $\Delta_p = (\Delta_p^+ - \Delta_p^-)/2$, where Δ_p^+ (Δ_p^-) is the energy of the coherence peak at positive (negative) sample bias. In order to calculate the average spectra for a given Δ_p , individual curves were first normalized, such that all have the same integral in the range $[-300, +300]$ mV. Figure 3 shows the set of individual and average spectra for Δ_p between 36 and 54 meV. Also shown is the standard deviation to the average, as a function of bias. For all Δ_p , the standard deviation is of the order of 5%, except close to the coherence peaks where it increases up to 20%.

The prominent spectral features of Bi-2223 are evident from the average differential conductance curves shown in Fig. 3. All spectra present a d -wave like spectral shape at low bias, very well developed coherence peaks at the gap edges, and a dip-hump structure at energies larger than Δ_p . These features, as we discuss in the following paragraphs, systematically evolve with Δ_p . Another remarkable property of the Bi-2223 spectra is a strong electron-hole asymmetry, characterized by a greater spectral weight for the occupied sample states. This is manifested by higher coherence peaks, and an enhanced conductance background at negative bias. Detected in most high- T_c 's, this phenomenology contrasts with the symmetric spectra of classical superconductors. The line-shape of the coherence peaks also follows a monotonic

trend with Δ_p , when considering its evolution for either negative or positive bias. The peaks sharpen and become taller on decreasing their energy location with respect to the Fermi level.

The electron-hole asymmetry monotonically evolves with Δ_p . Firstly, the conductance background for the occupied states becomes steeper on decreasing the gap. The trend is particularly evident when considering data in a bias range one order of magnitude larger than Δ_p . This evolution may be due to a variation of the correlation effects with the pairing strength.⁴⁴ Since our microscopic model does not consider such correlations, we will restrict our fits to the bias interval $[-150, +150]$ mV. Secondly, the asymmetry in the height of coherence peaks systematically increases when decreasing Δ_p . We will discuss the role of the Van Hove singularity in this phenomenology in Secs. III C and IV.

The evolution of the dip is of particular importance for this work. This feature consists in a local minimum of conductance at E_d , in the vicinity of the coherence peaks, outside the gapped region. In the case of Bi-2223, the dip feature is strongly developed in comparison to other Bi-based cuprates. The line-shape of this feature is noticeably electron-hole asymmetric, the dip being stronger in the occupied part of the spectrum. As we will discuss in the following sections, another important trend is the evolution of the energy separation $E_d - \Delta_p = \Omega_s$ with Δ_p : Ω_s decreases on increasing the gap.

Finally, the low-energy conductance is similar for all values of Δ_p . Close to the Fermi level, the spectra are electron-hole symmetric, and present a slightly rounded shape. A strictly V-shaped low bias conductance is expected for a d -wave superconductor at zero temperature. However, some rounding off and a finite zero-bias conductance are expected when considering thermal and measurement broadening, the latter due to the finite amplitude of the ac lock-in excitation, or to electronic noise. Our fitting procedure takes these two experimental factors into account.

III. MICROSCOPIC MODEL AND FITTING PROCEDURE

A. STM tunneling conductance and LDOS

The theory of tunneling in superconductors³⁸ was historically meant for planar junctions involving classical s -wave superconductors, with a structureless normal-state DOS. On the other hand, the theory of Tersoff and Hamann⁵¹ for the STM was not developed for superconductors. The approach of Ref. 51 is nevertheless easily extended to describe STM tunneling into superconductors,² and leads to the well-known paradigm that the differential conductance is a measure of the thermally-broadened electron LDOS:

$$\frac{dI(\mathbf{r})}{dV} = M \int_{-\infty}^{\infty} d\omega d\varepsilon N(\mathbf{r}, \omega) [-f'(\omega - \varepsilon)] g_{\sigma}(\varepsilon - eV). \quad (1)$$

$N(\mathbf{r}, \omega)$ is the sample LDOS at the position, \mathbf{r} , where the STM tip is located, f' is the derivative of the Fermi function,

and M is a tip-dependent constant. We have considered in Eq. (1) an additional broadening, in order to take into account the finite experimental resolution. This is modeled by a Gaussian function g_{σ} , with half width at half maximum σ . There are several sources of extrinsic broadening in the experiment, among which the most obvious are the lock-in ac modulation, and the averaging of several similar spectra (see Sec. III). The strict proportionality of dI/dV and $N(\mathbf{r}, eV)$ is achieved in the limits of zero temperature and $\sigma = 0$, where both $-f'$ and g_{σ} become delta functions.

When the work function of the junction is large compared with the typical energies of interest (in our case, 3 eV compared with 0.1–0.2 eV, see Fig. 1), it is reasonable to assume that all Bloch waves decay exponentially outside the sample surface, with the same energy-independent decay constant κ . The LDOS at the tip location \mathbf{r} reduces then to $N(\mathbf{r}, \omega) \propto \exp(-2\kappa z)N(\omega)$, with $N(\omega)$ the bulk two-dimensional DOS, assumed translation-invariant in the (x, y) plane. Consistently, the current must decrease exponentially with z , as confirmed in Fig. 1. The z -dependent factors, which are irrelevant in spectroscopic measurements, are lumped into the constant M of Eq. (1), where $N(\mathbf{r}, \omega)$ can thus be replaced by $N(\omega)$. We then calculate the two-dimensional DOS as the Brillouin-zone integral of the electron spectral function:

$$N(\omega) = \frac{2}{N} \sum_{\mathbf{k}} (-1/\pi) \text{Im} G_{11}(\mathbf{k}, \omega). \quad (2)$$

Here, G_{11} is the first component of the one-electron Green's function in the Nambu particle-hole representation, and N is the number of \mathbf{k} points in the two-dimensional Brillouin zone. In a superconductor characterized by a BCS gap $\Delta_{\mathbf{k}}$, and inelastic scattering processes, it is convenient to write G_{11} in terms of the 2×2 matrix self-energy $\hat{\Sigma}(\mathbf{k}, \omega)$, in the form

$$G_{11} = \left[\omega - \xi_{\mathbf{k}} + i\Gamma - \Sigma_{11} - \frac{(\Delta_{\mathbf{k}} + \Sigma_{12})^2}{\omega + \xi_{\mathbf{k}} + i\Gamma - \Sigma_{22}} \right]^{-1}. \quad (3)$$

$\Sigma_{11}(\mathbf{k}, \omega)$ and $\Sigma_{22}(\mathbf{k}, \omega)$ describe the renormalization and damping of the Bogoliubov quasiparticles in the electron and hole branches, respectively, while the ‘‘anomalous’’ self-energy $\Sigma_{12}(\mathbf{k}, \omega)$ describes inelastic-scattering effects in the pairing channel.⁵² The explicit form that we use for $\hat{\Sigma}$ is provided in the next subsection. If $\hat{\Sigma} = 0$, Eq. (3) reduces to the classical BCS Green's function, with $\xi_{\mathbf{k}} \equiv \varepsilon_{\mathbf{k}} - \mu$ the noninteracting electron dispersion, μ the chemical potential, and Γ a phenomenological constant scattering rate.⁵³ We use a tight-binding model for the band $\varepsilon_{\mathbf{k}}$, involving up to five-neighbor hopping, which reads (setting the lattice parameter $a \equiv 1$):

$$\begin{aligned} \varepsilon_{\mathbf{k}} \equiv \sum_{\mathbf{r}} t(|\mathbf{r}|) e^{i\mathbf{k} \cdot \mathbf{r}} &= 2t_1(\cos k_x + \cos k_y) + \\ &4t_2 \cos k_x \cos k_y + 2t_3(\cos 2k_x + \cos 2k_y) + \\ &4t_4(\cos 2k_x \cos k_y + \cos k_x \cos 2k_y) + \\ &4t_5 \cos 2k_x \cos 2k_y. \end{aligned} \quad (4)$$

Note that our conventions for the signs and magnitudes of the hopping amplitudes t_i differ from those used in Ref. 37. For the BCS gap, we assume a pure $d_{x^2-y^2}$ symmetry, i.e., $\Delta_{\mathbf{k}} = \Delta_0(\cos k_x - \cos k_y)/2$.

Bi-2223 has three CuO_2 layers per unit cell, and therefore displays three bands at the Fermi level.⁵⁴ We nevertheless use a one-band model. This model turns out to be appropriate for fitting the spectra in the range $[-150, +150]$ mV, and has the advantage of reducing the number of adjustable parameters. Recent photoemission studies suggested that the Bi-2223 band triplet is actually divided into a doublet of nearly degenerate bands, attributed to the two outer CuO_2 layers, and a single band at lower energy, associated with the inner CuO_2 layer.^{55,56} The inner-layer band is seen below the doublet, at ~ 70 meV in the nodal direction, and at an extrapolated energy of ~ 200 meV in the anti-nodal direction. Therefore, a one-band approximation focusing on the doublet is sufficient to fit our spectra, since the latter carries 2/3 of the spectral weight, and the Van Hove singularity of the inner-layer band lies ~ 200 meV below that of the doublet, just at the border of our measurement window. At low energies, we therefore expect that the modifications induced in the theoretical STM spectra by using a multi-band description would be marginal. That said, we point out that the average spectra displayed in Fig. 3 systematically present a weak structure between -215 and -225 mV, which might be the signature of the inner-layer Van Hove singularity. This is supported by the fact that the structure is only seen at negative bias. Although a definitive assessment is not possible at this stage, this observation confirms that possible multi-band effects are likely to be small.

B. Bogoliubov quasiparticles coupled to spin fluctuations

The theoretical investigation of the coupling between Bogoliubov quasiparticles and spin fluctuations began with the study of the superfluid transition in ^3He (see Ref. 57 and references therein), and was revived with the discovery of high- T_c superconductors.^{58–60} The minimal model to describe the effects of this coupling is

$$\hat{\Sigma}(\mathbf{k}, \omega) = -\frac{1}{N} \sum_{\mathbf{q}} \frac{1}{\beta} \sum_{i\Omega_n} g^2 \chi_s(\mathbf{q}, i\Omega_n) \times \hat{\mathcal{G}}_0(\mathbf{k} - \mathbf{q}, i\omega_n - i\Omega_n) \Big|_{i\omega_n \rightarrow \omega + i0^+}. \quad (5)$$

$\hat{\mathcal{G}}_0$ is the 2×2 Nambu-BCS-Matsubara Green's function in the absence of coupling, χ_s is the spin susceptibility, $i\omega_n$ and $i\Omega_n$ are the fermionic and bosonic Matsubara frequencies, respectively, $\beta = (k_B T)^{-1}$ is the inverse temperature, and g is the coupling parameter. Equation (5) can be obtained from perturbation theory in the electron-spin coupling;⁶¹ it can also be viewed as a simplified, non-self-consistent, version of a conserving strong-coupling theory.⁶²

Following Ref. 37, we use a separable phenomenological expression for χ_s in the superconducting state. In the energy range of interest, namely below ~ 150 meV, we assume that

the spin response is dominated by a resonance at energy Ω_s , near the antiferromagnetic vector $\mathbf{Q} = (\pi, \pi)$:

$$\chi_s(\mathbf{q}, i\Omega_n) = W_s F(\mathbf{q}) \int_{-\infty}^{\infty} d\varepsilon \frac{I(\varepsilon)}{i\Omega_n - \varepsilon}. \quad (6)$$

We choose the real functions $F(\mathbf{q})$ and $I(\varepsilon)$ such that $(1/N) \sum_{\mathbf{q}} F(\mathbf{q}) = \int_0^{\infty} d\varepsilon I(\varepsilon) = 1$. Thus, W_s stands for the momentum and frequency integrated spectral weight of the resonance:

$$W_s = \frac{1}{N} \sum_{\mathbf{q}} \int_0^{\infty} d\omega \left(-\frac{1}{\pi}\right) \text{Im} \chi_s(\mathbf{q}, \omega). \quad (7)$$

The function $F(\mathbf{q})$ is Lorentzian-like, peaked at $\mathbf{q} = \mathbf{Q}$, with a half width at half maximum Δq :

$$F(\mathbf{q}) = \frac{F_0}{\sin^2\left(\frac{q_x - Q_x}{2}\right) + \sin^2\left(\frac{q_y - Q_y}{2}\right) + (\Delta q/4)^2}. \quad (8)$$

The constant F_0 ensures the normalization of $F(\mathbf{q})$. In Ref. 37, the resonance was assumed to be sharp in energy, so that its energy distribution was $I(\varepsilon) = \delta(\varepsilon - \Omega_s) - \delta(\varepsilon + \Omega_s)$. Indeed, neutron scattering measurements suggest that the resonance is resolution-limited in Y-123.⁹ We have used a slightly more general form,

$$I(\varepsilon) = I_0 [L_{\Gamma_s}(\varepsilon - \Omega_s) - L_{\Gamma_s}(\varepsilon + \Omega_s)], \quad (9)$$

where $L_{\Gamma}(\varepsilon) = (\Gamma/\pi)/(\varepsilon^2 + \Gamma^2)$ is a Lorentzian, and I_0 ensures the normalization of $I(\varepsilon)$. The form (9) allows us to take into account a finite lifetime $\tau_s \sim \Gamma_s^{-1}$ of the spin excitation. Neutron scattering experiments indicate that the resonance is somewhat broader in Bi-2212 (Ref. 13) and Bi-2223 (Ref. 63) than in Y-123, and would be consistent with $\Gamma_s \approx 4\text{--}8$ meV. Alternatively, Eq. (9) may be regarded as a crude way to account for the experimentally observed dispersion of the resonance,⁶⁴ which would broaden the sharp mode into a band of width Γ_s .

It is convenient to write the Matsubara Green's function in Eq. (5) using the spectral representation:

$$\hat{\mathcal{G}}_0(\mathbf{k}, i\omega_n) = \int_{-\infty}^{\infty} d\varepsilon \frac{\hat{A}(\mathbf{k}, \varepsilon)}{i\omega_n - \varepsilon}. \quad (10)$$

Taking into account the phenomenological scattering rate Γ appearing in Eq. (3), the spectral function can be expressed in terms of Lorentzian functions as

$$\hat{A}(\mathbf{k}, \varepsilon) = \hat{u}_{\mathbf{k}} L_{\Gamma}(\varepsilon - E_{\mathbf{k}}) + \hat{v}_{\mathbf{k}} L_{\Gamma}(\varepsilon + E_{\mathbf{k}}), \quad (11)$$

where

$$\hat{u}_{\mathbf{k}} = \frac{1}{2} \begin{pmatrix} 1 + \frac{\xi_{\mathbf{k}}}{E_{\mathbf{k}}} & \frac{\Delta_{\mathbf{k}}}{E_{\mathbf{k}}} \\ \frac{\Delta_{\mathbf{k}}}{E_{\mathbf{k}}} & 1 - \frac{\xi_{\mathbf{k}}}{E_{\mathbf{k}}} \end{pmatrix}, \quad \hat{v}_{\mathbf{k}} = \mathbb{1} - \hat{u}_{\mathbf{k}}, \quad (12)$$

and $E_{\mathbf{k}} = \sqrt{\xi_{\mathbf{k}}^2 + \Delta_{\mathbf{k}}^2}$. Inserting Eqs. (6) and (10) into Eq. (5), one can perform the summation over Matsubara

frequencies using standard techniques,⁶⁵ and using Eqs. (9) and (11), one obtains the self-energy on the real-frequency axis:

$$\hat{\Sigma}(\mathbf{k}, \omega) = \frac{\alpha^2}{N} \sum_{\mathbf{q}} F(\mathbf{q}) [\hat{u}_{\mathbf{k}-\mathbf{q}} B(\omega, E_{\mathbf{k}-\mathbf{q}}) + \hat{v}_{\mathbf{k}-\mathbf{q}} B(\omega, -E_{\mathbf{k}-\mathbf{q}})]. \quad (13)$$

We have introduced the dimensionless coupling constant $\alpha^2 \equiv (g/\Lambda)^2 W_s I_0$, with Λ a characteristic energy scale of the model, which we take as the nearest-neighbor hopping t_1 . For definiteness, the function $B(\omega, E)$ is derived in the Appendix. The self-energy (13) is a convolution in momentum space, and can therefore be efficiently evaluated numerically on dense \mathbf{k} -point meshes using fast Fourier transforms.

The use of a dimensionless coupling constant α incorporating the spectral weight of the resonance, instead of the original coupling g like in Ref. 37, is more convenient for our purposes. The strength of the self-energy effects on low-energy Bogoliubov quasiparticles—hence the strength of the dip in the tunneling spectrum—is governed by the product $g^2 W_s$, and W_s strongly depends on the momentum width of the resonance, Δq . In the original formulation, both g and Δq strongly affect the dip strength, whereas, in our formulation, the dip strength is controlled mostly by α , and weakly depends on Δq . Since the model parameters will be determined by least-square fits to the experimental data, one may expect a simpler landscape if one avoids that different parameters have the same influence on the theoretical spectrum.

C. Discussion of the model

The model has fifteen parameters, including the multiplicative constant M in Eq. (1), thirteen of which are determined by least-square fitting. The two fixed parameters are the experimental temperature $T = 2$ K, and the Gaussian broadening σ in Eq. (1), set to 4 meV. The latter value represents the broadening effect of the lock-in modulation, and the average of several spectra to reduce the noise and produce representative spectra, as shown in Fig. 3. Additional broadening is provided by the Dynes parameter Γ , which accounts phenomenologically for impurity scattering, and varies between 1 and 9 meV in our fits. The main parameter is Δ_0 , which sets the scale of the d -wave gap. In this model, the d -wave gap is not assumed to result self-consistently from the coupling to spin fluctuations, in the fashion of the Eliashberg theory for phonons. Instead, it is assumed that a d -wave gap is preexisting, and that the coupling to the spin resonance comes as a perturbation. The effect of the spin resonance on pairing is discussed further below.

The band parameters t_{1-5} and the chemical potential μ determine the noninteracting DOS, the band filling, and the noninteracting Fermi surface. The property of the band on which the tunneling spectrum is most sensitive is the energy of the Van Hove singularity (VHS), equal to the dispersion at the M point $(\pi, 0)$, i.e., $\xi_M = 4(-t_2 + t_3 + t_5) - \mu$. The effect

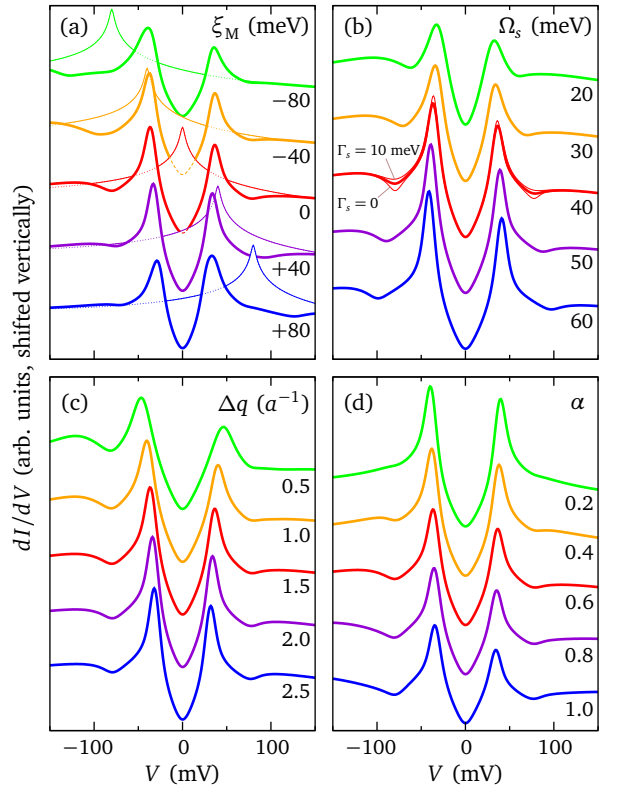


FIG. 4. Evolution of the theoretical tunneling spectrum with varying five relevant parameters of the model. The base parameters are (all energies are in meV) $M = 1$, $\Gamma = 2$, $t_{1-5} = (-250, 80, 0, 0, 0)$, $\mu = -320$, $\Delta_0 = 40$, $\Omega_s = 40$, $\Gamma_s = 5$, $\Delta_q = 1.5/a$, $\alpha = 0.6$, and they correspond to the middle red curve in each series. The \mathbf{k} -point mesh contains 1024×1024 points. In (a), the chemical potential is varied to move the Van Hove singularity with respect to zero energy from -80 to $+80$ meV; the thin lines show the corresponding noninteracting DOS. (b), (c), and (d) show the result of varying the mode energy Ω_s , the mode \mathbf{q} -space width Δq , and the coupling α , respectively. The effect of changing Γ_s is illustrated by the thin curves in (b).

of varying ξ_M is illustrated in Fig. 4(a). Four main trends can be observed: the position of the VHS affects (1) the difference in the heights of the two coherence peaks, (2) the electron-hole asymmetry of the dip, (3) the overall height of the coherence peaks, and (4) the half peak-to-peak gap Δ_p . (1) results from the opening of the superconducting gap, which pushes the VHS further down if initially located at negative energy, and further up in the opposite case. The coherence peak closest to the singularity thus carries more spectral weight. One notices that some electron-hole asymmetry remains when $\xi_M = 0$, even if the weight of the VHS is evenly distributed among the two coherence peaks. The reason is that the noninteracting DOS breaks electron-hole symmetry, since a $t_2 \neq 0$ produces an excess weight at negative energies. (2) is a consequence of the dip being reinforced by the VHS, and therefore being stronger at negative energy if $\xi_M < 0$, and vice-versa.³¹ (3) reflects the overall contribution of the VHS to the coherence peaks, so that the latter are tallest when $\xi_M = 0$. Lastly, (4) is a

consequence of the d -wave symmetry of the gap, implying that the maximum gap on the Fermi surface is generally smaller than Δ_0 , and decreases as the Fermi surface moves away from the M point.

The remaining four parameters characterize the spin resonance. Changing the resonance energy Ω_s has mainly three effects, as shown in Fig. 4(b): (1) the dip minimum moves with respect to the closest coherence peak, (2) the height of the coherence peaks changes, and (3) the gap size varies. (1) indicates that the damping of Bogoliubov excitations is strongest near the energy $\Delta_0 + \Omega_s$: excitations near this energy can easily decay by emitting a (π, π) spin mode, since there are many final states available near the gap-edge energy Δ_0 . In order to figure out the typical energy dependence of the electron scattering rate, $-\text{Im}\bar{\Sigma}_{11}(\mathbf{k}, \omega)$, one can use the simple limit of Eq. (A8) for the B function, and average Eq. (13) over the Brillouin zone, to arrive at

$$-\text{Im}\bar{\Sigma}_{11}(\omega) = \frac{\pi}{2}(\alpha t_1)^2 [\theta(\omega - \Omega_s)N_0(\omega - \Omega_s) + \theta(-\omega - \Omega_s)N_0(\omega + \Omega_s)], \quad (14)$$

where $N_0(\omega)$ is the d -wave BCS DOS. Since $N_0(\omega)$ has coherence peaks at $|\omega| \approx \Delta_0$, $-\text{Im}\bar{\Sigma}_{11}(\omega)$ peaks at $\omega \approx \pm(\Delta_0 + \Omega_s)$, leading to the occurrence of dips in the full DOS at these energies. The actual scattering rate has a marked \mathbf{k} -dependence,^{37,39} which is washed out in Eq. (14). The momentum dependence is due to the resonance being confined around (π, π) , and approximately amounts to inserting a \mathbf{k} -dependent amplitude in the right-hand side of Eq. (14). The latter still captures the correct qualitative energy dependence. The effect (2)—increase of the coherence peaks height with increasing Ω_s —can also be understood with the help of Eq. (14): the scattering rate vanishes in the energy range $|\omega| < \Omega_s$, where Bogoliubov quasiparticles cannot decay, and thus the coherence peaks are not broadened if $\Omega_s > \Delta_0$. The broadening of the coherence peaks is maximum when the peak in $-\text{Im}\bar{\Sigma}_{11}$ occurs at the energy Δ_p , i.e., when $\Omega_s \rightarrow 0$. The trend (3) has its origin in the renormalization of the quasiparticle energies, encoded in the real part of the self-energy. At low energy, we have $\text{Re}\bar{\Sigma}_{11}(\omega) \approx -\bar{\lambda}\omega$, so that the energy levels are renormalized by a factor $1/(1 + \bar{\lambda})$. Performing the Brillouin-zone average as above leads to

$$\bar{\lambda} = (\alpha t_1)^2 \frac{1}{2} \int_{-\infty}^{\infty} d\varepsilon \frac{N_0(\varepsilon)}{(|\varepsilon| + \Omega_s)^2}. \quad (15)$$

If the anti-nodal Fermi crossing is not too far from the M point, the scale Δ_p of the gap in the theoretical spectrum is given to a good approximation by $\Delta_0(1 + \Psi_M)/(1 + \lambda_M)$. λ_M is the renormalization at the M point, that is typically 30% larger than the Brillouin-zone average $\bar{\lambda}$, and $\Psi_M = \text{Re}\Sigma_{12}(M, 0)/\Delta_0$ gives the contribution of the anomalous self-energy to pairing. Ψ_M is a decreasing function of Ω_s ; this can be seen by estimating the Brillouin-zone average of $\text{Re}\Sigma_{12}(\mathbf{k}, 0)/\Delta_k$, which gives

$$\bar{\Psi} \approx (\alpha t_1)^2 \int_0^{\infty} d\varepsilon \frac{N_0(\varepsilon)}{\varepsilon(\varepsilon + \Omega_s)}. \quad (16)$$

Equation (16) is accurate in the limit $\Delta q \rightarrow 0$, and for a electron-hole symmetric band. From the Ω_s -dependence of $\bar{\Psi}$ alone, one would expect a decrease of Δ_p with increasing Ω_s . However, this is over-compensated by the faster decrease of $\bar{\lambda}$ with Ω_s [see Eq. (15)], so that the net result is a slight increase of Δ_p with increasing Ω_s , as seen in Fig. 4(b). Figure 4(b) also illustrates the effect of increasing the energy width Γ_s of the spin resonance: that is a broadening mostly confined to the neighborhood of the dip minimum.

Figure 4(c) shows that the momentum width Δq of the spin resonance mainly controls the gap renormalization. If $\Delta q \lesssim a^{-1}$, Ψ_M wins over λ_M , and consequently $\Delta_p > \Delta_0$, while the opposite occurs if $\Delta q \gtrsim a^{-1}$. The precise value of Δq for which this change of behavior takes place depends on the other model parameters. In the limit $\Delta q \rightarrow 0$, the renormalization parameters at M can be evaluated as

$$\lambda_M = \frac{(\alpha t_1)^2}{(E_M + \Omega_s)^2}, \quad \Psi_M = \frac{(\alpha t_1)^2}{E_M(E_M + \Omega_s)} \quad (\Delta q = 0), \quad (17)$$

and clearly $\Psi_M > \lambda_M$ in this case ($E_M = \sqrt{\xi_M^2 + \Delta_0^2}$). In the opposite limit, $\Delta q \rightarrow \infty$ or $F(\mathbf{q}) \equiv 1$, the self-energy becomes momentum independent. We then simply get

$$\lambda_M = \bar{\lambda}, \quad \Psi_M = 0 \quad (\Delta q = \infty), \quad (18)$$

such that the gap is reduced by a factor $1/(1 + \bar{\lambda})$ in this case. The vanishing of Ψ_M is a consequence of the d -wave symmetry of Δ_k . It is important to remember that the variation in Fig. 4(c) is performed at *fixed spectral weight* of the resonance. In other words, the bare coupling g decreases as Δq increases, so as to keep the α coupling unchanged.

Finally, changing the dimensionless coupling α produces a three-fold effect, as seen in Fig. 4(d): increasing α (1) digs the dip, (2) reduces the gap, and (3) lowers the coherence peaks without broadening them. (1) reflects the fact that the scattering rate is proportional to α^2 [Eq. (14)]. (2) results because $\Delta q > a^{-1}$ in Fig. 4(d), so that $\Psi_M < \lambda_M$, as discussed previously; since both Ψ_M and λ_M are proportional to α^2 , the quantity $(1 + \Psi_M)/(1 + \lambda_M)$ decreases with increasing α . Finally, the effect (3) is due to the fact that coupling to the spin resonance removes spectral weight at low energies, and transfers it to higher energies, not only over intermediate energy scales corresponding to the “hump”, but over a larger energy scale, up to the band edges. This is demonstrated in Fig. 5, which shows the data of Fig. 4(d) on an expanded energy scale. The transfer of spectral weight from low to high energies explains why the coherence peaks are lowered with increasing α . We further note that part of the spectral weight removed in the dip is also pushed to *lower* energies and, under certain conditions, can lead to shoulders on the sides of the coherence peaks.

We close this section with a few general remarks. Unlike in the strong-coupling theory for conventional superconductors, the model that we are using does not allow us to find a simple relationship between its parameters and the location of prominent features in the theoretical tunneling spectrum. The rule is that each feature is controlled in different ways by several parameters. For instance, the peak-to-peak gap

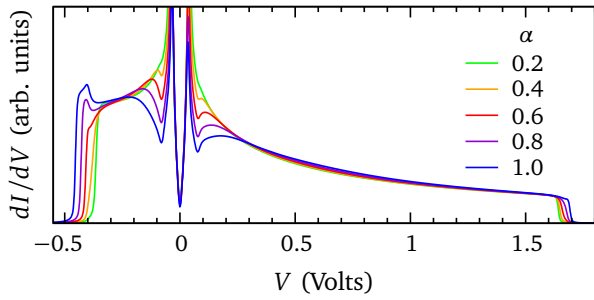


FIG. 5. Same data as Fig. 4(d) on an expanded energy scale covering the whole bandwidth. Part of the low-energy spectral weight is transferred to the band edges.

Δ_p depends on Δ_0 , ξ_M , Ω_s , Δq , and α , as illustrated in Fig. 4. A direct readout of the parameters from inspection of the spectra is therefore possible only qualitatively, and fitting is required for extracting accurate values. Yet, there is one peculiarity of the spectrum, which can be attributed to a single source: the electron-hole asymmetry—of the coherence peaks height, dip strength, and conductance background—is entirely due, in this model, to the electron-hole asymmetry of the underlying normal-state DOS. Therefore, the qualitative inference of an asymmetric normal DOS *can* be made by direct inspection of the spectra. Finally, we emphasize that, although the contribution of the anomalous self-energy to pairing is always positive, the experimental magnitude Δ_p may eventually turn out to be smaller than Δ_0 , due to the normal self-energy renormalization. Namely, the coupling to the spin resonance contributes positively to pairing, but can nevertheless reduce the preexisting gap.

D. Fitting procedure and accuracy of the parameters

The 13-parameter landscape is too complex for a blind brute-force fitting approach. It contains plenty of local minima, providing equally satisfactory fits “by the eye”, but parameters—especially band parameters—which are significantly different. The reason is that the theoretical spectrum does not depend critically on each hopping amplitude t_i separately, but rather on global properties of the noninteracting DOS, such as the position and asymmetry of the VHS, that are not in one-to-one correspondence with the set of t_i values. It is indeed possible to find different sets of hopping amplitudes, which give rise to noninteracting DOS curves that are hardly distinguishable in a limited energy window.⁶⁶ Hence the probability is close to one, that a least-square fit, starting with random values of the parameters, ends in some unphysical local minimum. It is even very likely that the absolute minimum, corresponding to the best fit in a mathematical sense, would provide for some parameters, values which must be excluded on physical grounds. Therefore, a pinch of physical common sense must be added to the procedure, and the fits can not be entirely automatic. Such “educated fits” are rather (human) time consuming, and can hardly be undertaken for a large number of spectra.

In a first step, we have focused our attention to the average spectra displayed in Fig. 3. For each of them, we searched a set of parameters which (i) is a minimum of the least-square function,⁶⁷ (ii) corresponds to a noninteracting band with plausible hopping parameters, and the properties shared by all Bi-based cuprates—band minimum at the Γ point, band maximum at the (π, π) point, VHS at the M point—and (iii) provides a hole-like Fermi surface centered at (π, π) . We have not constrained the band parameters in order to fix the carrier density, because the local density corresponding to each spectrum is unknown, and the nominal density deduced from the bulk T_c is not very meaningful in heterogeneous samples. The actual procedure has been to search good parameters for the spectra with $\Delta_p = 36$ and 54 meV (this required a bit of trial and error), and then to use interpolations between these parameters as seeds to fit the average spectra with intermediate gaps. The fits were restricted to the energy window $|\omega| < 150$ meV.

In a second step, we have estimated the uncertainty of the fitted parameters. There are standard statistical procedures to retrieve an uncertainty for parameters determined by a least-square fit. These uncertainties relate to the quality of that particular fit, but do not provide a meaningful estimate for the error bars to put on physical quantities in our case. Indeed, as we perform fits on average spectra, the dispersion of the physical parameters among the individual spectra has been removed. In order to get a better estimate of the error bars, we have fitted all individual spectra, using as seed values the parameters obtained for the corresponding average spectrum. These latter fits were not “educated”: each model parameter was left free to vary. As an illustration, Fig. 6 displays all individual spectra with an experimental gap of 44 meV, together with the fitted curves. From the

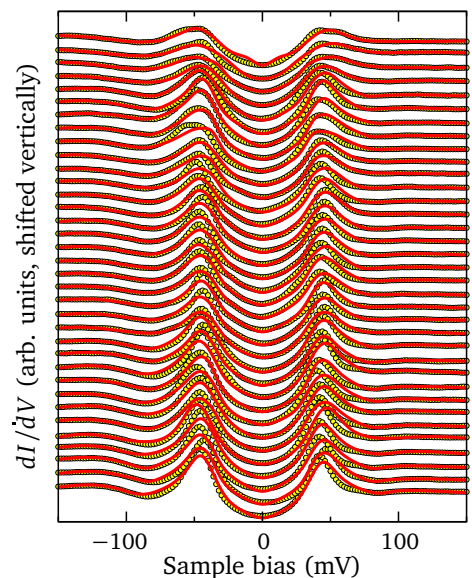


FIG. 6. Series of local experimental spectra with a peak-to-peak gap $\Delta_p = 44$ meV (yellow circles), and their fit to the microscopic model (red lines). Similar results are obtained for all series in Fig. 3.

distributions of fitted values in such series, we deduce an average and a standard deviation for each fitted parameter, which can be compared with the values obtained by fitting the average spectra.

IV. RESULTS

Figure 7 presents the results of our fits to the average spectra, and Table I lists the complete set of fitted parameters, as well as the estimated uncertainties. Considering the simplicity of the model—with regard to the high chemical and electronic complexity of the material—the quality of the fits in Fig. 7 is remarkable. The model reproduces the relative values of the conductance at zero bias, on the coherence peaks, and on the background, as they vary with increasing Δ_p . It also captures the electron-hole asymmetry of the coherence peaks, and the decrease of this asymmetry with increasing Δ_p . The electron-hole asymmetry of the dip can be followed as a function of Δ_p , even when the coherence peaks have become almost symmetric, at $\Delta_p = 54$ meV. The theoretical spectra are systematically too “V”-shaped near zero bias, as compared to the experimental ones that look more rounded, particularly for smaller Δ_p values. This might be an indication of a small deviation from pure $d_{x^2-y^2}$ -wave symmetry close to the gap nodes. Although we have restricted the fits to the low-energy region, it is also possible to obtain good fits in the full energy range of Fig. 3, at the price of a slight deterioration of the fit quality at low energies, especially for the largest gaps. The progressive inadequacy of the model for increasingly extended energy ranges can receive different explanations. One possibility is the presence of additional components in the experimental spectrum, not considered in the model, like the contribution of the inner-layer band and/or a correlation-induced excess of spectral weight for occupied states, which develops as Δ_p increases.⁴⁰ Another possibility is the existence of other scattering mechanisms at high energy, in particular the scattering on the continuum of spin fluctuations.³⁷

Before discussing the parameters reported in Table I, we emphasize three implications of Fig. 7. The excellent quality of the fits substantiates our basic assumption, that scanning tunneling spectroscopy measures the local electron DOS: the raw STS data can be directly compared with a model calculation based on physically plausible parameters. The presence of the Van Hove singularity in the noninteracting DOS is crucial to reproduce the various asymmetries of the spectra: the noninteracting dispersion is the *only* source of electron-hole symmetry breaking in this model. Finally, a coupling to the spin resonance can quantitatively explain the redistribution of spectral weight around the dip energy. The tight localization of the resonance around (π, π) , as opposed to optical phonons that span the whole Brillouin zone, plays a key role in producing the correct line-shape of the dip.

Inspecting Table I, one first notices that the values obtained by fitting the average spectra coincide, within the uncertainty, with the average of the values obtained by

fitting individual spectra. One also notices the large uncertainties, in some cases up to 100%, associated with the band parameters t_i , illustrating the weak sensitivity of the theoretical spectrum to each individual t_i (see Sec. III D). The nearest-neighbor hopping t_1 varies between -140 and -256 meV: these values are plausible, and fall within the range of published values for Bi-based cuprates.^{37,68,69} Physically, one does not expect large local variations of t_1 , such as those seen in Table I. It should be noted, however, that these variations are comparable with the typical uncertainty of t_1 . Furthermore, the set of fitted hopping parameters should not be regarded as an accurate determination of the microscopic hopping amplitudes, but rather as an effective representation of the low-energy dispersion. We will see below that the properties of the dispersion which have relevance close to the Fermi surface, such as the VHS energy and the Fermi velocity, have comparatively smaller uncertainties. The hopping amplitude t_3 to the second neighbor along the Cu-Cu axes is negative, like t_1 , as expected from symmetry considerations. Likewise, the diagonal hoppings t_2 and t_5 are both positive, or the latter is almost zero (we consider the small negative values of order 1 meV as insignificant).

The phenomenological scattering rate Γ remains small, with a tendency to increase for larger gaps. This variation allows us to capture part of the overall broadening of the spectra observed in the raw data with increasing Δ_p . Another part of this broadening, for $\Delta_p \geq 44$ meV is provided by a steep increase of the spin resonance width Γ_s . Values of ~ 15 meV for Γ_s seem somewhat too large, when compared with available values for Bi-2212 and Bi-2223,^{13,63} but we note that their uncertainty is also quite large. The uncertainty of Γ is comparatively smaller, because this parameter provides the only broadening mechanism at energies below Ω_s , and it is therefore well constrained by the line-shape around zero bias. We find that Δ_0 is 20 to 30% larger than Δ_p . As discussed in Sec. III C, a reduction of the bare gap occurs when Δq exceeds a critical value, and the pairing induced by the spin resonance is over-compensated by the downward renormalization of the energy levels. In our case, Δq shows a tendency to increase with increasing Δ_p , and correspondingly, the difference between Δ_0 and Δ_p also increases. The fitted Ω_s are anti-correlated with Δ_p , as discussed in more detail below, and consistently with previous studies.^{31,32} Lastly, the dimensionless coupling α exhibits no clear trend, but the product $(\alpha t_1)^2$, which controls the strength of the scattering rate [see, e.g., Eq. (14)], increases steadily with increasing Δ_p . We discuss the coupling strength further below.

V. DISCUSSION

A. Electron-hole asymmetry and Van Hove singularity

The tunneling spectra exhibit systematic asymmetries between positive and negative bias, suggestive of an intrinsic electron-hole asymmetry of the electron DOS. The asymmetries concern the height of the coherence peaks, the strength

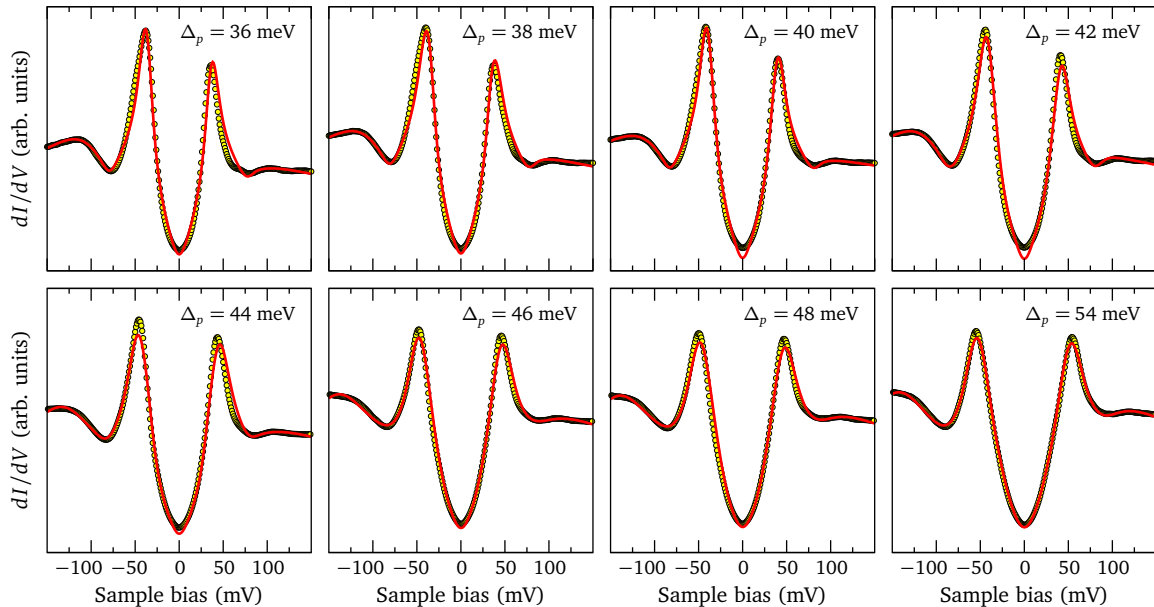


FIG. 7. Average spectra of Fig. 3 (circles) and fits with the microscopic model described in Sec. III (red curves). The model parameters are given in Table I (first column for each parameter).

TABLE I. Values of the model parameters obtained from fitting average and individual spectra. For each experimental gap Δ_p and each parameter, the first column gives the value obtained by fitting the average spectrum, as shown in Fig. 7; the second column gives the average of the values obtained by fitting all individual spectra, as illustrated in Fig. 6; the number in parentheses is the corresponding standard deviation.

Δ_p (meV)	Parameters of the noninteracting dispersion											
	μ (meV)		t_1 (meV)		t_2 (meV)		t_3 (meV)		t_4 (meV)		t_5 (meV)	
36	-165	-187 (56)	-180	-205 (43)	32	43(24)	-11	-6(10)	2.2	-2.7 (8.6)	-1.6	-0.7 (3.7)
38	-125	-164(111)	-161	-192 (79)	21	31(36)	-14	-11(17)	5.8	3.0 (9.3)	-1.4	-3.6 (6.3)
40	-101	-135(105)	-140	-176 (85)	3	21(46)	-23	-15(21)	11.9	3.7(15.5)	-3.4	-2.3 (4.1)
42	-116	-122 (51)	-162	-179 (46)	18	24(26)	-17	-15(13)	4.3	-0.8 (9.2)	-0.8	2.9 (3.5)
44	-237	-274(108)	-206	-247(217)	56	52(50)	-36	-64(93)	-10.3	-13.3(39.9)	27.9	42.3(42.0)
46	-306	-243 (73)	-179	-169 (66)	59	29(43)	-79	-93(49)	-22.6	-19.4(12.6)	56.6	55.1(16.6)
48	-340	-329(108)	-206	-206(109)	60	36(52)	-97	-129(55)	-26.3	-20.6 (9.3)	67.0	76.1(24.9)
54	-305	-296(146)	-256	-239 (87)	58	18(44)	-88	-134(73)	-35.4	-27.1(15.9)	62.9	69.7(25.6)

Δ_p (meV)	Scattering rate, BCS gap, and (π, π) resonance											
	Γ (meV)		Δ_0 (meV)		Ω_s (meV)		Γ_s (meV)		Δq (a^{-1})		α	
36	2.0	2.3(0.7)	42.7	42.3(1.0)	36.8	36.8(0.9)	1.6	1.8(1.1)	1.39	1.34(0.11)	0.73	0.67(0.14)
38	2.1	2.5(0.6)	45.0	46.0(3.7)	34.5	34.6(2.5)	0.5	1.0(1.1)	1.46	1.45(0.34)	0.79	0.76(0.19)
40	1.0	1.9(0.9)	47.9	46.7(3.4)	34.4	35.7(2.3)	1.7	2.2(2.1)	1.54	1.41(0.38)	0.97	0.88(0.29)
42	1.0	2.2(0.9)	52.5	49.1(4.9)	29.9	33.3(3.2)	1.7	2.3(2.1)	1.65	1.38(0.49)	0.81	0.78(0.18)
44	3.6	3.9(2.4)	48.6	47.7(7.3)	33.7	33.5(4.5)	4.2	4.1(5.4)	1.15	1.20(0.60)	0.70	0.72(0.27)
46	6.6	6.3(1.7)	59.7	64.0(6.4)	21.6	14.5(9.9)	18.6	18.3(7.0)	1.68	2.04(0.69)	1.16	1.65(0.32)
48	7.6	7.1(1.8)	60.4	61.7(5.9)	23.1	18.3(9.1)	15.1	14.1(7.2)	1.80	1.92(0.62)	0.97	1.31(0.38)
54	8.5	8.5(1.7)	70.7	71.8(6.3)	19.2	14.3(6.8)	13.7	14.0(8.0)	2.17	2.42(0.58)	0.79	1.13(0.35)

of the dip feature, and the conductance background. The three effects are present, with varying magnitudes, in all spectra, as highlighted in Fig. 8. In the model, any asymmetry can be traced back to the noninteracting band structure. In particular, there is a simple relationship between the

width and asymmetry of the dip, and the energy ξ_M of the VHS in the noninteracting band,³¹ as is clear from Fig. 4(a). A wider and/or stronger dip at negative bias implies $\xi_M < 0$. Furthermore, one generally finds that the negative-energy coherence peak is taller when $\xi_M < 0$, although this rule

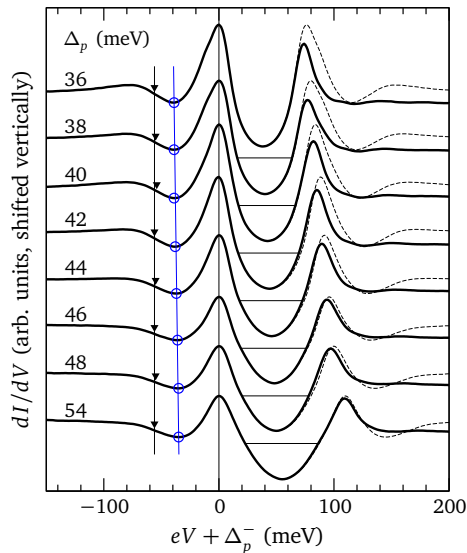


FIG. 8. Average experimental spectra of Fig. 3, with the energies measured from the maximum of the negative-bias coherence peak. The dashed lines show the negative-bias spectrum, mirrored at positive energies to highlight the electron-hole asymmetry. The circles indicate the dip minimum, the triangles show the inflection point (peak in d^2I/dV^2), and the straight lines are guides to the eye.

is not absolute [see Fig. 4(a)]. In this respect, the series of experimental spectra in Fig. 8 present two trends, which seem to have conflicting implications. On the one hand, the coherence peaks become more symmetric with increasing Δ_p , suggesting that ξ_M is negative for small gaps, and approaches zero for larger gaps. On the other hand, there is a tendency for the dip to become wider and more asymmetric with increasing Δ_p , indicating that the VHS moves to lower energies with increasing Δ_p .

The latter evolution is consistent with the interpretation that spectra with larger gaps correspond to more underdoped regions with higher electron densities. It is also supported by the fits, which yield larger negative values of ξ_M for larger gaps [see Fig. 9(a)]. Interestingly, by extrapolating our results, one expects a VHS at positive energy for gap values lower than 24 meV, i.e., on the strongly overdoped side. We are not aware of any systematic investigation of the VHS by angle-resolved photoemission (ARPES) in Bi-2223. One point of comparison is given by the analysis of Ref. 70, which leads to a dispersion approaching -25 meV at $(\pi, 0)$, the value that we obtain for gaps close to 45 meV. However, this analysis neglects renormalization effects, and may therefore underestimate ξ_M .

B. Spin-resonance energy

Figure 9(b) shows the fitted values of Ω_s . For the smallest gaps, corresponding to spectra with tall and asymmetric coherence peaks, we find values between 30 and 40 meV, and a good correspondence between the Ω_s obtained from

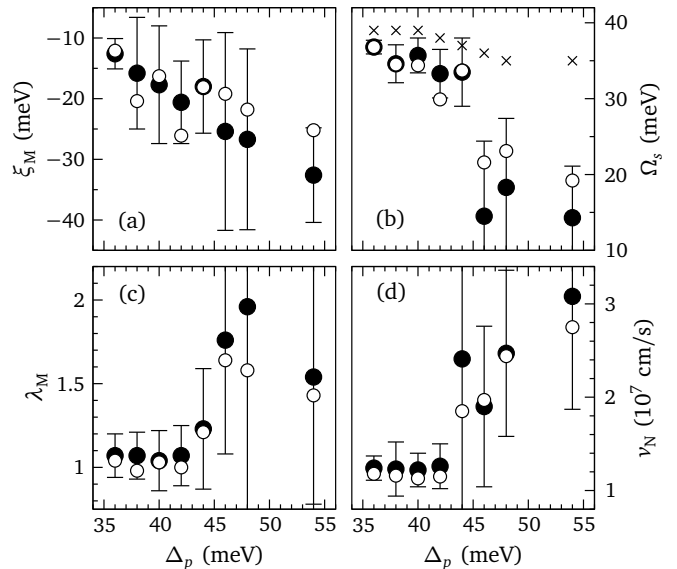


FIG. 9. Physical parameters, as determined by the fits. The full symbols with error bars show the average parameters and their standard deviation, obtained by fitting all individual spectra. The empty symbols show the parameters obtained by fitting the average spectra. The crosses in (b) represent the peak-to-dip energy difference $E_d - \Delta_p$ of the experimental average spectra, corresponding to the circles in Fig. 8. (c) Renormalization factor, Eq. (19), at the M point $(\pi, 0)$. (d) Nodal velocity.

the fits, and the peak-to-dip energy difference, the latter being a few meV larger than the former. Both magnitudes follow the same decreasing trend with increasing Δ_p . We stress that the spectral feature corresponding to a peak in the second derivative spectrum d^2I/dV^2 occurs at a significantly higher energy of 56 meV (triangles in Fig. 8), similar to the values observed in Bi-2212 (Ref. 71). Therefore, the peak in d^2I/dV^2 does not provide a good estimate of Ω_s . This is a hallmark of the d -wave gap symmetry, and occurs irrespective of the nature of the collective mode.^{36,39} For gaps larger than 45 meV, the fitted Ω_s drop abruptly to values close to 20 meV, in contrast to the peak-to-dip energies in the experimental spectra, that stay close to 35 meV. We presume that part of this drop is driven by changes in the tunneling spectra, which go beyond the scope of the model: the rapid drop of Ω_s is accompanied by other changes, such as a sudden raise of Γ_s and t_5 (see Table I), suggesting that the fit has been pushed to a different region of the parameter space.

Inspecting the data, one sees that an obvious change between the 44 and 46 meV spectra is a falloff of the peak to background ratio. This modification cannot be accounted for by simply increasing Γ and/or Γ_s , since this would also reduce the dip to background ratio, while in the spectra the latter remains unchanged. The compromise found by the fitting routine is to lower Ω_s , and thus to reduce the peaks' height without affecting the dip strength [see Fig. 4(b)], and to tune the position of the dip minimum by adjusting other parameters [in particular, increasing Δq pushes up

the ratio Δ_0/Δ_p , and increases the peak-to-dip separation as seen in Fig. 4(c)]. Another trend is that the coherence peaks become symmetric for large gaps, and this also drives Ω_s downward in the fits.

In the absence of neutron scattering data for Ω_s in Bi-2223, and considering the large uncertainty in the fitted values for Δ_p larger than 45 meV, it is difficult to ascertain whether the actual decrease of the spin-resonance energy for large gaps is as sudden as suggested by our fits, or rather more continuous. Nevertheless, the range of values which we find corresponds well to the doping evolution observed in Y-123, where the resonance energy decreases from ~ 40 meV at optimal doping to 25 meV in underdoped samples.^{72,73} In Bi-2212, the resonance is found at 42 meV at optimal doping, and its energy decreases down to 34 meV with strong overdoping,¹³ but no data has been so far reported in the underdoped region.

C. Coupling strength and renormalization factors

The values of the bare coupling strength obtained from our fits, i.e., g in Eq. (5), are similar to those used in Ref. 37. However, as discussed in Sec. III, comparing the bare couplings obtained by fitting different spectra can be misleading, because the strength of the strong-coupling effects depends also on other model parameters, particularly on the momentum spread Δq of the resonance. A physically meaningful measure of the coupling strength is provided by the renormalization factor, which we define as

$$\lambda_k = -\frac{d}{d\omega} \frac{1}{2} [\Sigma_{11}(\mathbf{k}, \omega) + \Sigma_{22}(\mathbf{k}, \omega)]_{\omega=0}. \quad (19)$$

The Brillouin-zone average of this quantity is given approximately by Eq. (15). The evolution of λ_k at the M point with varying Δ_p is shown in Fig. 9(c): λ_M increases sharply at $\Delta_p = 45$ meV. Like for Ω_s , the λ_M error bars are larger for the spectra with larger gaps. The renormalization λ_k is anisotropic in momentum space, as shown in Fig. 10. The values of λ_k are smaller in the nodal region than close to the anti-nodal points. The figure also shows that, for the smallest gaps, the Fermi surface average of λ_k (dots) is well approximated by the full Brillouin-zone average (horizontal bars) given by Eq. (15). For larger gaps, the Fermi surface moves away from the M point, where the renormalization is strongest and, as a result, $\bar{\lambda}$ is larger than the average Fermi-surface renormalization. We note that the expression (17), valid for $\Delta q = 0$, overestimates λ_M by a factor ~ 2.5 for small gaps, where Δq is smallest, and by a factor ~ 3.5 for the larger gaps with larger Δq values. The formula (17) should therefore be used with caution, unless Δq is very small. The fast increase of λ_M above $\Delta_p = 45$ meV is accompanied by an increase of anisotropy: the difference in renormalization between anti-nodal and nodal regions is 20–30% for the smaller gaps, and increases to 30–50% for the larger gaps. Note that the λ_k shown in Fig. 10(a) are significantly larger, and more anisotropic, than the values found for Bi-2212 using phonon models.⁷⁴ This suggests that

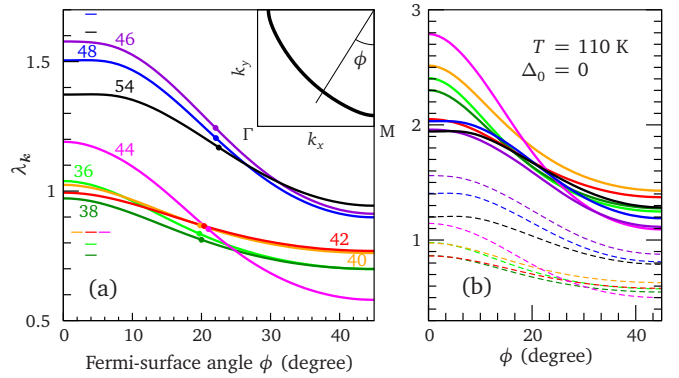


FIG. 10. Renormalization factor λ_k on the renormalized Fermi surface. (a) Superconducting state: the parameters are those corresponding to the average spectra of Fig. 7 with the corresponding value of Δ_p written on each curve. The dots indicate the Fermi-surface average of λ_k , and the horizontal bars show the Brillouin-zone average calculated with Eq. (15) (off-scale for $\Delta_p = 46$ meV). Inset: Fermi surface for $\Delta_p = 42$ meV, and definition of the Fermi-surface angle ϕ . (b) Normal state: the solid lines show the value of λ_k obtained by setting $\Delta_0 = 0$ and $T = 110$ K, and keeping the other parameters unchanged. The dashed lines correspond to $\Delta_0 = 0$, $T = 110$ K, and $\Gamma_s = 25$ meV.

fitting our STM data to phonon-based models would lead to unrealistically large electron-phonon matrix elements.

The experimental determination of λ by ARPES and optical conductivity are often performed in the normal state. In view of a comparison with those data, we note that the calculated λ 's increase significantly on going from the superconducting to the normal state. This can be understood by looking at Eq. (15), which shows that $\bar{\lambda}$ increases as the gap in $N_0(\epsilon)$ closes. Figure 10(b) displays the λ values computed at the Bi-2223 critical temperature $T_c = 110$ K, with Δ_0 set to zero, while keeping the other parameters unchanged. The renormalization increases by a factor 1.2–2.4 with respect to its value in the superconducting state, and the anisotropy also raises up to 30–60%. Experimentally, the transition to the normal state also affects the spin resonance, which broadens in energy⁷⁵ on warming across T_c . This can be modeled by increasing the value of Γ_s , while keeping the other parameters fixed. In the absence of experimental input on the normal-state value of Γ_s in Bi-2223, we show in Fig. 10(b), as an illustration, the normal-state renormalization calculated with $\Gamma_s = 25$ meV. The values of the renormalization are reduced by the increase of Γ_s , and are similar to the values calculated in the superconducting state if $\Gamma_s = 25$ meV.

Our renormalization factors compare well with experimental values reported in the literature. In underdoped and overdoped Bi-2212, the normal-state renormalization near the anti-nodal point, determined by photoemission, was found to be 1.5.²⁶ This is consistent with our finding $\lambda_M \approx 2$, considering that the more pronounced dip feature in the STM spectra of Bi-2223 with respect to Bi-2212 indeed points to a larger coupling in the three-layer compound. In the normal state, but at the nodal point, a renormalization

decreasing from 0.8 to 0.55 as a function of increasing hole doping was measured at $T = 120$ K in Bi-2212.⁷⁶ Our nodal values for Bi-2223 in the normal state, and for $\Gamma_s = 25$ meV, decrease from 0.8 to 0.5 with decreasing gap size, which draws a similar trend as observed in Bi-2212. Below T_c , nodal values of λ between 0.7 and 0.9 for Bi-2212 are reported in Ref. 76, very close to our superconducting-state results of Fig. 10(a). In photoemission experiments, an accurate determination of the anti-nodal renormalization at low temperature is difficult, due to the presence of the superconducting gap. A detailed study reported a value of 2 for optimally-doped Bi-2212,⁷⁷ while our values for Bi-2223 vary between 1 and 1.6. To our knowledge, no ARPES value of λ has been explicitly reported for Bi-2223. Nevertheless, from a recent study,⁷⁸ we may estimate a nodal λ of 0.6 at 10 K for an optimally-doped sample, which lies at the lower edge of our values in Fig. 10(a). Finally, the average renormalization factor in the normal state of optimally-doped Bi-2223 has been estimated by fitting optical data³⁵ to a model involving a spectrum of bosonic excitations, and lead to the values 2.18 and 1.75, depending whether the full bosonic spectrum, or only its low-energy part, is taken into account, respectively. Both values fall within our range of normal-state renormalizations in Fig. 10(b).

Figure 9(d) shows the nodal velocity, calculated using the parameters obtained from the fits, and assuming a Bi-2223 in-plane lattice constant of 3.825 Å. The nodal velocity can be directly measured by ARPES, unlike the renormalization λ_k , which requires assumptions about the noninteracting dispersion. Ref. 78 reports nodal velocities between 1.5 and 1.7 eV Å for the outer-layer band of optimally-doped Bi-2223, i.e., 2.3 – 2.6×10^7 cm/s. These values agree well with our results for $\Delta_p \gtrsim 44$ meV. In the case of Bi-2212, values ranging between 1 and 2.5×10^7 cm/s as a function of doping have been reported.⁷⁹ We conclude that the variations seen in Fig. 9(d) are consistent with variations of the nodal velocity associated with changes in the local doping level.

D. Spectral function and simulated ARPES intensity

The parameters determined by fitting STM spectra allow us to calculate the momentum-resolved spectral function, and to make predictions for the measured ARPES intensity. The generic properties of the spectral function in the present model have been extensively discussed.^{20,37} The main characteristics are summarized in Fig. 11. At energies below the onset of scattering, $|\omega| < \Omega_s$, the dispersion is renormalized downwards, but not broadened. This can be seen most clearly along the nodal direction $(0,0)$ – (π,π) in Fig. 11(a). At these low energies, the quasiparticles form banana-shaped regions around the nodal points [Fig. 11(b)]. Increasing energy from the onset of scattering at Ω_s , the scattering rate increases, and reaches its maximum at $\Delta_0 + \Omega_s$ [see Eq. (14)]. Since $\Delta_p \ll \Delta_0 + \Omega_s$, the anti-nodal excitations at $|\omega| = \Delta_p$ remain rather sharp [Fig. 11(c)]. When the scattering rate is maximum at $|\omega| = \Delta_0 + \Omega_s$, in con-

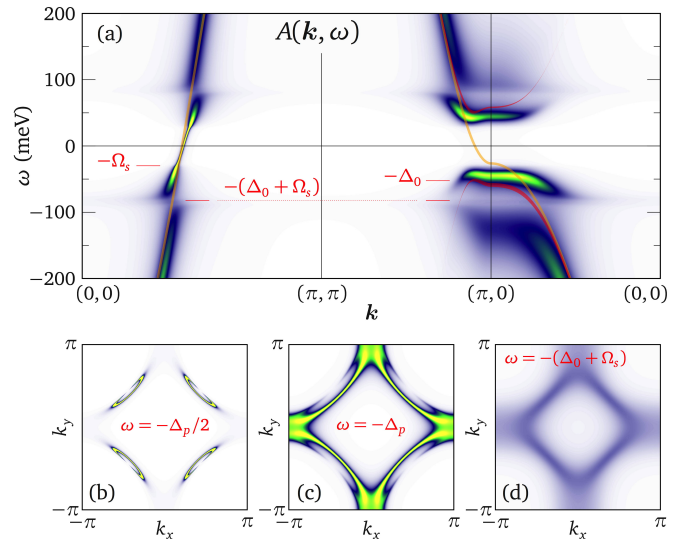


FIG. 11. Spectral function calculated using the parameters corresponding to the average spectrum with $\Delta_p = 42$ meV in Fig. 7. (a) Along high-symmetry lines in the Brillouin zone. The color scale shows the variation of the spectral function from zero (white) to its maximum (yellow). The orange line is the noninteracting dispersion. The red line shows the BCS dispersion; the width of the line is proportional to the spectral weight. (b), (c), and (d) Cuts at three characteristic energies. The color scale is the same in all graphs.

trast, the excitations are very broad [Fig. 11(d)]. At this energy, the real part of the self-energy changes sign, and the quasiparticle dispersion correspondingly jumps from below to above the noninteracting dispersion. This abrupt change in dispersion renormalization occurs at the same energy in the whole Brillouin zone, both for occupied and empty states, and leads to a suppression of states which is responsible for the dip in the DOS. Near the anti-node, the d -wave gap induces additional structures: the minimum-gap locus is close to—but not exactly at—the position of the noninteracting Fermi surface along the $(\pi,0)$ – (π,π) line, due to Fermi-surface renormalization. One also notices the reduction of the gap Δ_p , as compared to the BCS gap Δ_0 , due to the competition between pairing and renormalization, as discussed in Secs. III C and IV. In the low-energy region, the weakly-dispersing quasiparticle branch near $(\pi,0)$ has lower energy than the corresponding BCS branch, while above the dip energy, the quasiparticle energy is higher than the noninteracting and BCS dispersions, like in the nodal region.

In order to quantitatively compare our results with real ARPES data, we have used our model to simulate the upper panels of Fig. 2 in Ref. 80. With the aim of reproducing the experimental conditions of this work, we set the temperature to 10 K, and filter our spectral function with a Gaussian representing an energy resolution of 18 meV, and a momentum resolution of $0.05/a$.⁸⁰ The result is displayed in Fig. 12. Close to the nodal direction (left and middle panels), the agreement is good. The model—which only includes the spin resonance—is too crude to completely cap-

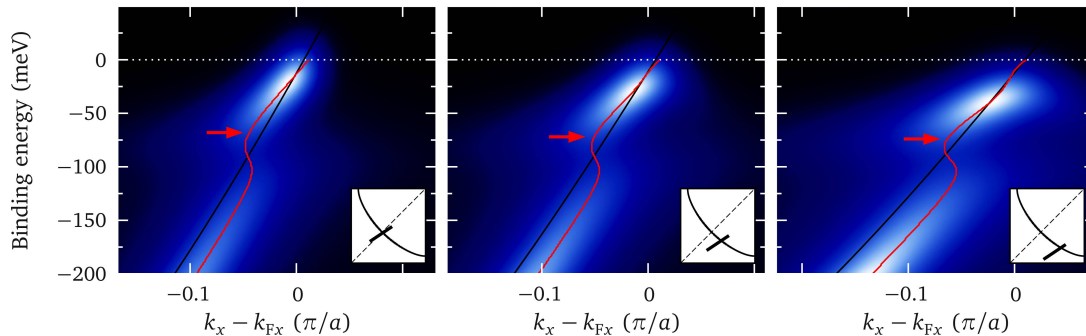


FIG. 12. Simulated ARPES intensity for optimally-doped Bi-2223 at temperature $T = 10$ K. The spectral function of Fig. 11 was multiplied by the Fermi function, and filtered to mimic a momentum resolution of $0.05/a$ and an energy resolution of 18 meV. The color scale and the three momentum cuts correspond approximately to those of Fig. 2 in Ref. 80. The black and red lines show the noninteracting and quasiparticle dispersions, respectively. The arrows indicate the “kink”, where the quasiparticle dispersion deviates from its low-energy linear behavior.

ture the measured dispersion in the region of the dip: in this energy range, the simulated dispersion jumps from below to above the noninteracting dispersion, while the experiment interpolates smoothly across the jump. We attribute this discrepancy to additional scattering mechanisms, not included in our model, in particular those involving the continuum of spin fluctuations.³⁷

The energy of the “kink”, around -70 meV, is well reproduced by the calculation. We note, however, that the feature corresponding to the energy $\Delta_0 + \Omega_s$ is *not* the kink, but the midpoint of the jump, where the quasiparticle dispersion crosses the noninteracting dispersion. It is also worth mentioning that this energy is not dispersing, and is given by $\Delta_0 + \Omega_s$, in spite of the fact that the gap vanishes at the node, as emphasized in Fig. 11(a). The experimental determination of this energy scale by ARPES requires an assumption for the shape of the noninteracting dispersion. Our results call into question the assumption made in Ref. 80, namely that the quasiparticle and noninteracting dispersions meet near -200 meV. This assumption has direct implications on the value of the self-energy derived from ARPES data, in particular, on the energy at which the real part vanishes. The value near -200 meV reported in Ref. 78 is obviously a direct consequence of the assumption made for the noninteracting dispersion. Using the dispersion resulting from our fits, one would be lead to the conclusion that the real part of the self-energy derived from ARPES vanishes at the energy $-(\Delta_0 + \Omega_s)$. In the anti-nodal region (right panel of Fig. 12), there are differences between our results and the ARPES data: the low-energy part, below the kink, is too dispersive in the model, while the high-energy part is not dispersive enough. This could be partly due to different Fermi surfaces in the experiment and in the model, which imply that the segments of the dispersion considered in the experiment and in the model are not exactly identical. It could also be the consequence of high-energy scattering processes, neglected in the model. Despite these differences, the kink energy and the minimum in the spectral intensity, between the low-energy and high-energy parts, are very similar in the simulation and in the experiment. The overall

agreement between Fig. 12 and Fig. 2 of Ref. 80 support the claim that STM tunneling spectra, although they come from a momentum-integrating probe, do contain the necessary information needed to reconstruct the low-energy momentum-resolved spectral function.

VI. SUMMARY AND CONCLUSIONS

We have performed an analysis of STM spectra measured on optimally-doped Bi-2223, by means of a microscopic model which takes into account the Van Hove singularity within a one-band description, a BCS gap with pure d -wave symmetry, and a coupling to the (π, π) spin resonance. This model can reproduce the experimental spectra remarkably well (Fig. 7), and provides values for the relevant physical parameters that are sound, and consistent with values obtained by other experimental probes. The inhomogeneity of the electronic properties observed on the sample surface allowed us to study variations in parameters as a function of the spectral gap Δ_p . Assuming a one-to-one correspondence between Δ_p and the hole doping level, changes in Δ_p may be interpreted as variations of local doping. The main trends are that the Van Hove singularity moves to lower energies, and the energy of the spin resonance decreases, with increasing Δ_p (Fig. 9). The former supports the interpretation that larger gaps correspond to lower dopings, and the latter supports the claim that the dip is caused by the spin resonance, rather than by optical phonons. The strength of the coupling to the spin resonance, measured by the dispersion renormalization, increases steadily for gaps larger than 42 meV, namely towards the underdoped region of the phase diagram.

The presence of a Van Hove singularity, breaking the electron-hole symmetry of the electronic spectrum, is unmistakable in the raw data (Fig. 8). Nevertheless, the precise determination of the hopping amplitudes t_i remains a challenge, as illustrated by the large uncertainties attached to these parameters in Table I. The reason is that relatively large variations of the t_i 's can collaborate to induce marginal

changes in the electron DOS, which largely govern the STM spectrum. Our confidence in the fitted tight-binding dispersion stems from the ability of the whole model to reproduce momentum-resolved ARPES data with good accuracy. In turn, our determination of the band-structure may provide indications on how to extract the self-energy from ARPES measurements.

ACKNOWLEDGMENTS

We acknowledge useful discussions with M. Eschrig. This work was supported by the Swiss National Science Foundation through Division II and MaNEP.

Appendix A: The function $B(\omega, E)$

Equations (5) to (11) imply that the function $B(\omega, E)$ entering Eq. (13) reads

$$B(\omega, E) = \Lambda^2 \int_{-\infty}^{\infty} d\varepsilon_1 d\varepsilon_2 [L_{\Gamma_s}(\varepsilon_1 - \Omega_s) - L_{\Gamma_s}(\varepsilon_1 + \Omega_s)] \times L_{\Gamma}(\varepsilon_2 - E) \frac{b(\varepsilon_1) + f(-\varepsilon_2)}{\omega - \varepsilon_1 - \varepsilon_2 + i0^+}, \quad (\text{A1})$$

where b and f are the Bose and Fermi functions, respectively. Using the identity $\int dx L_{\Gamma}(x)/(z - x) = 1/[z + i\Gamma \text{sign}(\text{Im}z)]$, we obtain

$$\Lambda^{-2}B(\omega, E) = \int_{-\infty}^{\infty} d\varepsilon \frac{L_{\Gamma_s}(\varepsilon - \Omega_s)b(\varepsilon)}{\omega - E + i\Gamma - \varepsilon} + \int_{-\infty}^{\infty} d\varepsilon \frac{L_{\Gamma}(\varepsilon - E)f(-\varepsilon)}{\omega - \Omega_s + i\Gamma_s - \varepsilon} - \{\Omega_s \rightarrow -\Omega_s\}. \quad (\text{A2})$$

The symbol in braces means that the result obtained from the first two terms on the r.h.s. must be anti-symmetrized with respect to Ω_s . The remaining integrals can be evaluated by closing the integration contour in the complex plane. The integrands can be rewritten in terms of products of simple

poles by means of the identities

$$L_{\Gamma}(z) = \frac{1}{2\pi i} \left(\frac{1}{z - i\Gamma} - \frac{1}{z + i\Gamma} \right) \quad (\text{A3})$$

$$b(z) = \frac{1}{\beta} \sum_{i\Omega_n} \frac{e^{i\Omega_n 0^+}}{z - i\Omega_n} \quad (\text{A4})$$

$$f(z) = -\frac{1}{\beta} \sum_{i\omega_n} \frac{e^{i\omega_n 0^+}}{z - i\omega_n}. \quad (\text{A5})$$

Only one half of the poles of the Bose or Fermi function are enclosed in the contour and give a contribution. Therefore, the integrals involve semi-infinite sums over Matsubara frequencies, which can be converted into the digamma function ψ , using the relation

$$\lim_{M \rightarrow \infty} \sum_{n=0}^M \frac{e^{\pm in 0^+}}{n + z} = \ln M - \psi(z). \quad (\text{A6})$$

The final result is

$$\begin{aligned} \Lambda^{-2}B(\omega, E) = & \frac{b(\Omega_s - i\Gamma_s) + \frac{1}{2\pi i} \psi \left[\frac{\beta}{2\pi i} (\Omega_s - i\Gamma_s) \right]}{\omega - E - \Omega_s + i(\Gamma + \Gamma_s)} \\ & + \frac{\frac{\Gamma_s}{\pi} \psi \left[\frac{\beta}{2\pi i} (\omega - E + i\Gamma) \right]}{(\omega - E - \Omega_s + i\Gamma)^2 + \Gamma_s^2} - \frac{\frac{1}{2\pi i} \psi \left[\frac{\beta}{2\pi i} (\Omega_s + i\Gamma_s) \right]}{\omega - E - \Omega_s + i(\Gamma - \Gamma_s)} \\ & + \frac{f(-E + i\Gamma) + \frac{1}{2\pi i} \psi \left[\frac{1}{2} + \frac{\beta}{2\pi i} (E - i\Gamma) \right]}{\omega - E - \Omega_s + i(\Gamma + \Gamma_s)} \\ & + \frac{\frac{\Gamma}{\pi} \psi \left[\frac{1}{2} + \frac{\beta}{2\pi i} (\omega - \Omega_s + i\Gamma_s) \right]}{(\omega - E - \Omega_s + i\Gamma_s)^2 + \Gamma^2} - \frac{\frac{1}{2\pi i} \psi \left[\frac{1}{2} + \frac{\beta}{2\pi i} (E + i\Gamma) \right]}{\omega - E - \Omega_s + i(\Gamma_s - \Gamma)} \\ & - \{\Omega_s \rightarrow -\Omega_s\}. \quad (\text{A7}) \end{aligned}$$

The function B simplifies considerably in the case of a sharp resonance ($\Gamma_s = 0^+$) and for sharp Bogoliubov quasiparticles ($\Gamma = 0^+$), as well as zero temperature. In this case, we have

$$B(\omega, E) = \frac{\Lambda^2}{\omega - E - \Omega_s \text{sign}(E) + i0^+}, \quad (\text{A8})$$

as can be readily deduced from Eq. (A1), by replacing the Lorentzians by delta functions.

* Present address: Low Temperatures Lab, Centro Atómico Bariloche, Argentina.

† Present address: Department of Physics and Astronomy, University of British Columbia, Vancouver, British Columbia V6T 1Z1, Canada.

¹ A. Damascelli, Z. Hussain, and Z.-X. Shen, *Rev. Mod. Phys.* **75**, 473 (2003).

² Ø. Fischer, M. Kugler, I. Maggio-Aprile, C. Berthod, and C. Renner, *Rev. Mod. Phys.* **79**, 353 (2007).

³ A. Piriou, N. Jenkins, C. Berthod, I. Maggio-Aprile, and Ø. Fischer, *Nat. Comm.* **2**, 221 (2011).

⁴ J. W. Alldredge, J. Lee, K. McElroy, M. Wang, K. Fujita, Y. Kohsaka, C. Taylor, H. Eisaki, S. Uchida, P. J. Hirschfeld, and J. C. Davis, *Nat. Phys.* **4**, 319 (2008).

⁵ I. Giaever, H. R. Hart, Jr., and K. Megerle, *Phys. Rev.* **126**, 941 (1962).

⁶ W. L. McMillan and J. M. Rowell, *Phys. Rev. Lett.* **14**, 108 (1965).

⁷ Y. Fasano, I. Maggio-Aprile, N. D. Zhigadlo, S. Katrych, J. Karpinski, and O. Fischer, *Phys. Rev. Lett.* **105**, 167005 (2010).

⁸ S. Chi, S. Grothe, R. Liang, P. Dosanjh, W. N. Hardy, S. A. Burke, D. A. Bonn, and Y. Pennec, *Phys. Rev. Lett.* **109**, 087002 (2012).

- ⁹ J. Rossat-Mignod, L. P. Regnault, C. Vettier, P. Bourges, P. Burlet, J. Bossy, J. Y. Henry, and G. Lapertot, *Physica C* **185**, 86 (1991).
- ¹⁰ H. A. Mook, M. Yethiraj, G. Aeppli, T. E. Mason, and T. Armstrong, *Phys. Rev. Lett.* **70**, 3490 (1993).
- ¹¹ G. Yu, Y. Li, E. M. Motoyama, X. Zhao, N. Barišić, Y. Cho, P. Bourges, K. Hradil, R. A. Mole, and M. Greven, *Phys. Rev. B* **81**, 064518 (2010).
- ¹² H. He, P. Bourges, Y. Sidis, C. Ulrich, L. P. Regnault, S. Pailhès, N. S. Berzigiarova, N. N. Kolesnikov, and B. Keimer, *Science* **295**, 1045 (2002); B. Keimer, H. He, P. Bourges, Y. Sidis, C. Ulrich, L. P. Regnault, S. Pailhès, N. S. Berzigiarova, and N. N. Kolesnikov, *J. Phys. Chem. Solids* **63**, 2243 (2002).
- ¹³ H. F. Fong, P. Bourges, Y. Sidis, L. P. Regnault, A. Ivanov, G. D. Gu, N. Koshizuka, and B. Keimer, *Nature* **398**, 588 (1999); L. Capogna, B. Fauqué, Y. Sidis, C. Ulrich, P. Bourges, S. Pailhès, A. Ivanov, J. L. Tallon, B. Liang, C. T. Lin, A. I. Rykov, and B. Keimer, *Phys. Rev. B* **75**, 060502 (2007); B. Fauqué, Y. Sidis, L. Capogna, A. Ivanov, K. Hradil, C. Ulrich, A. I. Rykov, B. Keimer, and P. Bourges, *Phys. Rev. B* **76**, 214512 (2007).
- ¹⁴ J. Mesot, N. Metoki, M. Böhm, A. Hiess, and K. Kadowaki, *Physica C* **341**, 2105 (2000).
- ¹⁵ G. Xu, G. D. Gu, M. Hücker, B. Fauqué, T. G. Perring, L. P. Regnault, and J. M. Tranquada, *Nat. Phys.* **5**, 642 (2009).
- ¹⁶ S. D. Wilson, P. Dai, S. Li, S. Chi, H. J. Kang, and J. W. Lynn, *Nature* **442**, 49 (2006).
- ¹⁷ Y. Sidis, S. Pailhès, B. Keimer, P. Bourges, C. Ulrich, and L. P. Regnault, *Phys. Status Solidi B* **241**, 1204 (2004).
- ¹⁸ H. He, Y. Sidis, P. Bourges, G. D. Gu, A. Ivanov, N. Koshizuka, B. Liang, C. T. Lin, L. P. Regnault, E. Schoenherr, and B. Keimer, *Phys. Rev. Lett.* **86**, 1610 (2001).
- ¹⁹ C. Stock, W. J. L. Buyers, R. Liang, D. Peets, Z. Tun, D. Bonn, W. N. Hardy, and R. J. Birgeneau, *Phys. Rev. B* **69**, 014502 (2004).
- ²⁰ See e.g. M. Eschrig, *Adv. Phys.* **55**, 47 (2006), and references therein.
- ²¹ P. W. Anderson, *Science* **317**, 1705 (2007).
- ²² T. A. Maier, D. Poilblanc, and D. J. Scalapino, *Phys. Rev. Lett.* **100**, 237001 (2008).
- ²³ H.-Y. Kee, S. A. Kivelson, and G. Aeppli, *Phys. Rev. Lett.* **88**, 257002 (2002).
- ²⁴ A. Abanov, A. V. Chubukov, M. Eschrig, M. R. Norman, and J. Schmalian, *Phys. Rev. Lett.* **89**, 177002 (2002).
- ²⁵ M. R. Norman, H. Ding, J. C. Campuzano, T. Takeuchi, M. Randeria, T. Yokoya, T. Takahashi, T. Mochiku, and K. Kadowaki, *Phys. Rev. Lett.* **79**, 3506 (1997); J. C. Campuzano, H. Ding, M. R. Norman, H. M. Fretwell, M. Randeria, A. Kaminski, J. Mesot, T. Takeuchi, T. Sato, T. Yokoya, T. Takahashi, T. Mochiku, K. Kadowaki, P. Guptasarma, D. G. Hinks, Z. Konstantinovic, Z. Z. Li, and H. Raffy, *Phys. Rev. Lett.* **83**, 3709 (1999); A. Kaminski, M. Randeria, J. C. Campuzano, M. R. Norman, H. Fretwell, J. Mesot, T. Sato, T. Takahashi, and K. Kadowaki, *Phys. Rev. Lett.* **86**, 1070 (2001).
- ²⁶ T. K. Kim, A. A. Kordyuk, S. V. Borisenko, A. Koitzsch, M. Knupfer, H. Berger, and J. Fink, *Phys. Rev. Lett.* **91**, 167002 (2003); S. V. Borisenko, A. A. Kordyuk, T. K. Kim, A. Koitzsch, M. Knupfer, J. Fink, M. S. Golden, M. Eschrig, H. Berger, and R. Follath, *Phys. Rev. Lett.* **90**, 207001 (2003); V. B. Zabolotnyy, S. V. Borisenko, A. A. Kordyuk, J. Fink, J. Geck, A. Koitzsch, M. Knupfer, B. Büchner, H. Berger, A. Erb, C. T. Lin, B. Keimer, and R. Follath, *Phys. Rev. Lett.* **96**, 037003 (2006); S. V. Borisenko, A. A. Kordyuk, A. Koitzsch, J. Fink, J. Geck, V. Zabolotnyy, M. Knupfer, B. Büchner, H. Berger, M. Falub, M. Shi, J. Krempasky, and L. Patthey, *Phys. Rev. Lett.* **96**, 067001 (2006).
- ²⁷ A. D. Gromko, A. V. Fedorov, Y.-D. Chuang, J. D. Koralek, Y. Aiura, Y. Yamaguchi, K. Oka, Y. Ando, and D. S. Dessau, *Phys. Rev. B* **68**, 174520 (2003).
- ²⁸ T. Sato, H. Matsui, T. Takahashi, H. Ding, H.-B. Yang, S.-C. Wang, T. Fujii, T. Watanabe, A. Matsuda, T. Terashima, and K. Kadowaki, *Phys. Rev. Lett.* **91**, 157003 (2003).
- ²⁹ J. F. Zasadzinski, L. Ozyuzer, N. Miyakawa, K. E. Gray, D. G. Hinks, and C. Kendziora, *Phys. Rev. Lett.* **87**, 067005 (2001); J. F. Zasadzinski, L. Coffey, P. Romano, and Z. Yusof, *Phys. Rev. B* **68**, 180504(R) (2003).
- ³⁰ B. W. Hoogenboom, C. Berthod, M. Peter, Ø. Fischer, and A. A. Kordyuk, *Phys. Rev. B* **67**, 224502 (2003).
- ³¹ G. Levy de Castro, C. Berthod, A. Piriou, E. Giannini, and Ø. Fischer, *Phys. Rev. Lett.* **101**, 267004 (2008).
- ³² N. Jenkins, Y. Fasano, C. Berthod, I. Maggio-Aprile, A. Piriou, E. Giannini, B. W. Hoogenboom, C. Hess, T. Cren, and Ø. Fischer, *Phys. Rev. Lett.* **103**, 227001 (2009).
- ³³ F. C. Niestemski, S. Kunwar, S. Zhou, S. Li, H. Ding, Z. Wang, P. Dai, and V. Madhavan, *Nature* **450**, 1058 (2007).
- ³⁴ J. P. Carbotte, E. Schachinger, and D. N. Basov, *Nature* **401**, 354 (1999); J. J. Tu, C. C. Homes, G. D. Gu, D. N. Basov, and M. Strongin, *Phys. Rev. B* **66**, 144514 (2002); J. Hwang, T. Timusk, and G. D. Gu, *Nature* **427**, 714 (2004); J. Yang, J. Hwang, E. Schachinger, J. P. Carbotte, R. P. S. M. Lobo, D. Colson, A. Forget, and T. Timusk, *Phys. Rev. Lett.* **102**, 027003 (2009).
- ³⁵ E. van Heumen, E. Muhlethaler, A. B. Kuzmenko, H. Eisaki, W. Meevasana, M. Greven, and D. van der Marel, *Phys. Rev. B* **79**, 184512 (2009); E. van Heumen, W. Meevasana, A. B. Kuzmenko, H. Eisaki, and D. van der Marel, *New J. Phys.* **11**, 055067 (2009).
- ³⁶ T. P. Devereaux, T. Cuk, Z.-X. Shen, and N. Nagaosa, *Phys. Rev. Lett.* **93**, 117004 (2004); S. Johnston and T. P. Devereaux, *Phys. Rev. B* **81**, 214512 (2010); S. Johnston, W. S. Lee, Y. Chen, E. A. Nowadnick, B. Moritz, Z.-X. Shen, and T. P. Devereaux, *Advances in Condensed Matter Physics* **2010**, 968304 (2010).
- ³⁷ M. Eschrig and M. R. Norman, *Phys. Rev. Lett.* **85**, 3261 (2000); *Phys. Rev. B* **67**, 144503 (2003).
- ³⁸ J. R. Schrieffer, D. J. Scalapino, and J. W. Wilkins, *Phys. Rev. Lett.* **10**, 336 (1963).
- ³⁹ C. Berthod, *Phys. Rev. B* **82**, 024504 (2010).
- ⁴⁰ M. Kugler, G. Levy de Castro, E. Giannini, A. Piriou, A. A. Manuel, C. Hess, and Ø. Fischer, *J. Phys. Chem. Solids* **67**, 353 (2006).
- ⁴¹ T. Sato, H. Matsui, S. Nishina, T. Takahashi, T. Fujii, T. Watanabe, and A. Matsuda, *Phys. Rev. Lett.* **89**, 067005 (2002).
- ⁴² D. L. Feng, A. Damascelli, K. M. Shen, N. Motoyama, D. H. Lu, H. Eisaki, K. Shimizu, J.-i. Shimoyama, K. Kishio, N. Kaneko, M. Greven, G. D. Gu, X. J. Zhou, C. Kim, F. Ronning, N. P. Armitage, and Z.-X. Shen, *Phys. Rev. Lett.* **88**, 107001 (2002).
- ⁴³ H. Matsui, T. Sato, T. Takahashi, H. Ding, H.-B. Yang, S.-C. Wang, T. Fujii, T. Watanabe, A. Matsuda, T. Terashima, and K. Kadowaki, *Phys. Rev. B* **67**, 060501(R) (2003).
- ⁴⁴ P. W. Anderson and N. P. Ong, *J. Phys. Chem. Solids* **67**, 1 (2006); P. W. Anderson, *Int. J. Mod. Phys. B* **25**, 1 (2011).
- ⁴⁵ M. Kugler, C. Renner, V. Mikheev, G. Batey, and Ø. Fischer, *Rev. Sci. Instrum.* **71**, 1475 (2000).
- ⁴⁶ E. Giannini, V. Garnier, R. Gladyshevskii, and R. Flükiger, *Supercond. Sci. Technol.* **17**, 220 (2004).
- ⁴⁷ A. Piriou, Y. Fasano, E. Giannini, and Ø. Fischer, *Phys. Rev. B* **77**, 184508 (2008).
- ⁴⁸ E. Giannini, N. Clayton, N. Musolino, A. Piriou, R. Gladyshevskii, and R. Flükiger, *IEEE Trans. Appl. Supercond.* **15**, 3102 (2005).

- ⁴⁹ E. Giannini, R. Gladyshevskii, N. Clayton, N. Musolino, V. Garnier, A. Piriou, and R. Flükiger, *Curr. App. Phys.* **8**, 115 (2008).
- ⁵⁰ A. Piriou, Y. Fasano, E. Giannini, and Ø. Fischer, *Physica C* **460-462**, 408 (2007).
- ⁵¹ J. Tersoff and D. R. Hamann, *Phys. Rev. Lett.* **50**, 1998 (1983).
- ⁵² There is a slight difference between Eq. (3), and the corresponding Eq. (7) of Ref. 30. The correct form of the self-energy requires the square of $\Delta_k + \Sigma_{12}$, like in Eq. (3), not the modulus square. The reason is that the Nambu self-energy is symmetric, $\Sigma_{12} = \Sigma_{21}$, but not hermitic.
- ⁵³ R. C. Dynes, V. Narayanamurti, and J. P. Garno, *Phys. Rev. Lett.* **41**, 1509 (1978).
- ⁵⁴ M. Mori, T. Tohyama, and S. Maekawa, *Phys. Rev. B* **66**, 064502 (2002).
- ⁵⁵ S. Ideta, K. Takashima, M. Hashimoto, T. Yoshida, A. Fujimori, H. Anzai, T. Fujita, Y. Nakashima, A. Ino, M. Arita, H. Namatame, M. Taniguchi, K. Ono, M. Kubota, D. H. Lu, Z.-X. Shen, K. M. Kojima, and S. Uchida, *Phys. Rev. Lett.* **104**, 227001 (2010); *Physica C* **470**, S14 (2010).
- ⁵⁶ P. Xu, *Photoemission Spectroscopy of Low-Dimensional Charge-Density-Wave and Superconducting Materials*, Ph.D. thesis, EPFL (2010).
- ⁵⁷ L. Tewordt, *J. Low Temp. Phys.* **15**, 349 (1973).
- ⁵⁸ D. J. Scalapino, E. Loh, and J. E. Hirsch, *Phys. Rev. B* **34**, 8190 (1986).
- ⁵⁹ S. Lenck, S. Wermbter, and L. Tewordt, *J. Low Temp. Phys.* **80**, 269 (1990).
- ⁶⁰ P. Monthoux, A. V. Balatsky, and D. Pines, *Phys. Rev. Lett.* **67**, 3448 (1991).
- ⁶¹ P. Monthoux, *Phys. Rev. B* **70**, 144403 (2004).
- ⁶² S. Wermbter and L. Tewordt, *Physica C* **211**, 132 (1993).
- ⁶³ S. Pailès, *Etude des excitations magnétiques dans le supraconducteur à haute température critique $Y_{1-x}Ca_xBa_2Cu_3O_{7-\delta}$* , Ph.D. thesis, Université Paris 6 (2004).
- ⁶⁴ P. Bourges, Y. Sidis, H. F. Fong, L. P. Regnault, J. Bossy, A. Ivanov, and B. Keimer, *Science* **288**, 1234 (2000); D. Reznik, P. Bourges, L. Pintschovius, Y. Endoh, Y. Sidis, T. Masui, and S. Tajima, *Phys. Rev. Lett.* **93**, 207003 (2004).
- ⁶⁵ G. D. Mahan, *Many Particle Physics*, 3rd ed. (Plenum, New York, 2000).
- ⁶⁶ For instance, the widely different sets of band parameters $(\mu, t_1, t_2, t_3, t_4, t_5) = (-192, -250, 52, -16, 2, 13)$ meV and $(-12, -158, 4, -6, 6, 0)$ meV yield almost identical noninteracting DOS curves, up to a multiplicative constant, in the energy range $|\omega| < 150$ meV.
- ⁶⁷ The usual least-square function, $F = \sum_i (y_i - Y_i)^2$, measures the vertical distance between two curves $y_i(x_i)$ and $Y_i(X_i)$. This is not ideal for curves with nearly vertical segments, like steep coherence peaks: in this case, a tiny horizontal mismatch is strongly penalized in the least-square function. For such situations, we use a different measure of the distance between two curves: for each point of the first curve, we take the shortest cartesian distance to any point of the second curve: $\tilde{F} = \sum_i \min_k [(x_i - X_k)^2 + (y_i - Y_k)^2]$. We minimize these functions with the Levenberg-Marquardt algorithm.
- ⁶⁸ M. R. Norman, M. Randeria, H. Ding, and J. C. Campuzano, *Phys. Rev. B* **52**, 615 (1995).
- ⁶⁹ A. A. Kordyuk, S. V. Borisenko, M. Knupfer, and J. Fink, *Phys. Rev. B* **67**, 064504 (2003).
- ⁷⁰ H. Matsui, T. Sato, T. Takahashi, S.-C. Wang, H.-B. Yang, H. Ding, T. Fujii, T. Watanabe, and A. Matsuda, *Phys. Rev. Lett.* **90**, 217002 (2003).
- ⁷¹ J. Lee, K. Fujita, K. McElroy, J. A. Slezak, M. Wang, Y. Aiura, H. Bando, M. Ishikado, T. Masui, J. X. Zhu, A. V. Balatsky, H. Eisaki, S. Uchida, and J. C. Davis, *Nature* **442**, 546 (2006).
- ⁷² P. Bourges, L. P. Regnault, J. Y. Henry, C. Vettier, Y. Sidis, and P. Burlet, *Physica B* **215**, 30 (1995).
- ⁷³ H. F. Fong, B. Keimer, D. L. Milius, and I. A. Aksay, *Phys. Rev. Lett.* **78**, 713 (1997).
- ⁷⁴ S. Johnston, F. Vernay, B. Moritz, Z.-X. Shen, N. Nagaosa, J. Zaanen, and T. P. Devereaux, *Phys. Rev. B* **82**, 064513 (2010).
- ⁷⁵ L. P. Regnault, P. Bourges, P. Burlet, J. Y. Henry, J. Rossat-Mignod, Y. Sidis, and C. Vettier, *Physica B* **213**, 48 (1995).
- ⁷⁶ A. A. Kordyuk, S. V. Borisenko, V. B. Zabolotnyy, J. Geck, M. Knupfer, J. Fink, B. Büchner, C. T. Lin, B. Keimer, H. Berger, A. V. Pan, S. Komiya, and Y. Ando, *Phys. Rev. Lett.* **97**, 017002 (2006).
- ⁷⁷ J. Fink, A. Koitzsch, J. Geck, V. Zabolotnyy, M. Knupfer, B. Büchner, A. Chubukov, and H. Berger, *Phys. Rev. B* **74**, 165102 (2006).
- ⁷⁸ S. Ideta, T. Yoshida, M. Hashimoto, A. Fujimori, H. Anzai, A. Ino, M. Arita, H. Namatame, M. Taniguchi, K. Takashima, K. M. Kojima, and S. Uchida, *arXiv:1208.6442* (2012).
- ⁷⁹ I. M. Vishik, W. S. Lee, R.-H. He, M. Hashimoto, Z. Hussain, T. P. Devereaux, and Z.-X. Shen, *New J. Phys.* **12**, 105008 (2010).
- ⁸⁰ S. Ideta, K. Takashima, M. Hashimoto, T. Yoshida, A. Fujimori, M. Kubota, K. Ono, K. Kojima, and S. Uchida, *J. Phys.: Conf. Ser.* **108**, 012015 (2008).